PFC/RR-90-4 DOE/PC-70512-16

Develop and Test an Internally Cooled, Cabled Superconductor (ICCS) for Large Scale MHD Magnets

Final Report
Contract No. DE-AC22-84PC70512

P.G. Marston, J.R. Hale, A.M. Dawson
30 April 1990

Plasma Fusion Center
Massachusetts Institute of Technologyy
Cambridge, Massachusetts 02139, USA

This work was supported by the U.S. Department of Energy, Pittsburgh Energy Technology Center, Pittsburgh, PA 15236, under Contract No. DE-AC22-84PC70512. Reproduction. translation, publication, use and disposal, in whole or part, by or for the United States Government is permitted.

Table of Contents

Executive Summary

The work conducted under DOE/PETC Contract DE-AC22-84PC70512 has included four principal tasks, 1) development of a Design Requirements Definition for a retrofit MHD magnet system, 2) analysis of an internally cooled, cabled superconductor (ICCS) to use in that design, 3) design of an experiment to test a subscale version of that conductor, which is a NbTi, copper stabilized superconductor, and 4) proof-of-concept testing of the conductor.

The program was carried forth through the third task with very successful development and test of a conventional ICCS conductor with 27 multifilamentary copper-superconductor composite strands and a new concept conductor in which, in each triplet, two strands were pure copper and the third strand was a multifilamentary composite. Tests were very successful, indicating that the latter conductor could be used effectively and would most probably be less expensive to manufacture.

In reviewing the magnet design and the premises for the conductor design it became obvious that, since the principal source of perturbation in MHD magnets derives from slippage between coils, or between turns in a coil, thereby producing frictional heat which must flow through the conductor sheath and the helium to the superconducor strands, an extra barrier might be highly effective in enhancing magnet stability and protection. This concept was developed and a sample conductor manufactured and tested in comparison with an identical conductor lacking such an additional barrier. Results of these conductor tests confirm the potential value of such a barrier. As the work of tasks 1 through 3 has been reported in detail in quarterly and semiannual reports, as well as in special reports prepared throughout the course of this project, this report reviews early work briefly and then discusses this last phase in great detail.

Glossary

Cu:SC (Cu/sc)	Copper-to-Superconductor ratio
Current sharing	The separation of the total current flowing in a conductor into two parts—one portion flows in the superconducting material without loss, and the other, 'shared' portion flows in the normal material (typically copper), generating joule heating. [This occurs whenever the temperature of the conductor exceeds T_{cs}.]
Filament	A sequence of straight-line current-carrying segments called 'Sticks,' from which a computer model of a magnet system can be built up. Many adjacent wires in an actual magnet can be represented in such a Stick Model by a single filament.
I_c	Critical Current of a superconductor, a function of magnetic field and temperature.
ICCS	Internally Cooled Cabled Superconductor.
I_{op}	Operating Current.
K	Kelvin(s), the SI unit of temperature; the SI unit of temperature interval.
kA	kiloamperes, or 1000 amperes.
L	Inductance; the SI unit is the henry.
MJ	megajoule, or 10^6 joules.
MPa	megapascal, 10^6 pascals; the SI unit of pressure is the pascal, one newton/m^2.
MW	megawatts, or 10^6 watts.
N	number of turns in a magnet coil or in a set of coils.
NbTi	Niobium-Titanium, a superconducting metal alloy.
Niobium-Tin	A superconducting intermetallic compound, Nb_3Sn.
Pancake	One type of magnet winding configuration, in which successive turns lie in the same plane at ever increasing radii, that is, in a plane spiral.
POC	Proof of Concept.
protection	The term applied in superconducting magnet technology to engineering design efforts to minimize or eliminate the potential for damage to, or destruction of, a magnet system in the event of a quench.
quench	The term applied to the complex sequence of phenomena that occurs whenever a superconducting magnet undergoes a nonrecoverable transition from the superconducting state to the normal state as a result

	of absorbing a heat perturbation that exceeds the stability margin (see Stability margin', below).
Shot	Term used in data acquisition to identify an 'event,' typically one that is initiated by the experimenter, as by discharging a capacitor, ramping a background magnetic field, etc.
stability	The term applied to a superconductor, or to a superconducting magnet, characterizing its resistance against, or susceptibility to quenching, that is, its sensitivity to heat perturbations.
Stability margin	The maximum amount of energy that can be deposited within a magnet, typically at the point where it is most vulnerable (as at the site of highest field), which will not initiate a quench.
Stick model	A type of computer model that approximates an actual magnet winding geometry by utilizing a set of straight segments, or sticks, as current-carrying elements. The straight sticks may be connected to one another to form current 'filaments'. Each filament in the stick model typically represents several turns in the actual magnet, thereby reducing the time required for field and force calculations. A stick model of a circular solenoid, for example, would be a set of n-sided polygons, where n is typically 10—20.
T	Tesla, the SI unit of magnetic induction.
T_{cs}	Current-sharing temperature, the temperature beyond which the operating current, that is, the total current flowing in a superconducting magnet, cannot be sustained wholly in the superconducting portion of a composite conductor, the result being that a portion of the current flows in (is 'shared' by) the resistive portion (typically copper) of the composite, generating joule heating in the conductor.
tonne	Metric ton, 1000 kilograms.
T_{op}	Operating temperature.

List of Figures

1.0 Introduction

The goal of this program, initiated in FY84, has been the proof-of-concept (POC) development and demonstration of a high-current internally cooled, cabled niobium-titanium (NbTi) superconductor for use in winding retrofit-scale MHD magnets. After preliminary design of such a magnet system, two subscale conductors were chosen for evaluation. Both were successfully tested. This work has established that significant cost savings may be realized in the manufacture of high copper-to-superconductor ratio ICCS conductors by demonstrating that cables having two out of every three strands made from copper worked as well as cables having all strands made from multifilamentary copper-superconductor composites. The overall copper-to-superconductor ratio was the same in both cables.

During the course of this work, a new ICCS conductor configuration for DC applications (DC-CICC) was conceived. In CY1988 considerable effort was put into the analysis of this new conductor concept, and CY1989 has been spent in extended preliminary analysis, and design and performance of the proof-of-concept tests of two embodiments of this conductor. This new conductor has the unique feature of having the protection function included in the conduit or sheath of the conductor rather than in the cable itself. This is permissible and, in fact, preferable because the main source of disturbance in MHD windings comes from turn-to-turn or layer-to-layer motion in the winding, rather than from wire motion in the superconducting cable.

2.0 Background

In the existing technology for coal-fired open-cycle MHD systems, a major concern is the constructability of large-scale (retrofit and then commercial scale) superconducting MHD magnets at an acceptable level of risk and with long-term structural durability. The development of a high-current conductor for the magnet winding, together with appropriate winding construction techniques and structural support criteria, are essential first steps in the technology effort required prior to beginning the final design and construction of a retrofit-scale magnet. The ICCS concept, which has been under development at MIT for a number of years is, for many reasons, a promising candidate for this application. The goal of this research program has been to translate the existing, fusion-related niobium-tin ICCS technology base into a NbTi base useful to the MHD community, and to further that technology through proof-of-concept testing of two 10-m lengths of prototypical conductor. The program elements have been: conceptual design of a retrofit-size MHD magnet to serve as the basis for the conductor design requirements definition; establishment of conductor design requirements; analysis to support the design effort; and finally, subscale experimental testing and proof-of-concept testing.

3.0 Discussion of Work Completed

3.1 Design Requirements Definition

The selection of magnet size and field strength was supported by information obtained from the MHD community as reported previously[1]. The selection of a relatively high design current is in the interest of minimum overall system cost, based on information provided in Reference 3. The selection of the particular ICCS overall dimensions and construction method is aimed at minimizing conductor development time and cost by using a conductor size and construction method for which production and tooling experience already exist.

An initial preconceptual design for a retrofit-size magnet was generated, incorporating a 60° rectangular saddle-coil winding of ICCS, without substructure, operating at a design current of 24 kA and surrounded by a stainless-steel force containment structure and cryostat. This design is discussed in detail in Reference 6.

A detailed computer analysis of the winding showed maximum fields to be somewhat higher than originally estimated (approaching 7.2 T instead of the estimated 6 T), requiring that the design be modified to reduce the maximum field and ensure stable operation.

Several winding design modifications, aimed at reducing the maximum field, were then analyzed. Modifications included changing the shape of the end turns, changing the aspect ratio of the winding cross section, and decreasing the winding average current density. A reduction of maximum field to below 6.9 T was found to be possible. A revised winding design having an increased thickness, an increased bend radius in the end turns, and a lower current density was established as most suitable for the application. Characteristics of the revised design and also of the original design are given below:

	Original	Revised
Coil Thickness (m)	0.24	0.305
Minimum End Turn Bend Radius (m)	0.15	0.30
Winding Average Current Density (A/cm^2)	3900	3200
Design Current in Conductor (kA)	24	18
Maximum Field in Winding (T)	7.2 (Orig. est 6.0)	6.9

In order to establish a conductor Design Requirements Definition, it is necessary to know the design characteristics of the magnet in which the conductor is intended to operate. Since a suitable reference design for a retrofit-size MHD magnet did not exist when the program was started, the development of a preconceptual design for such a magnet was a major effort.

The end product of the work was an improved magnet preconceptual design which compared favorably with earlier magnet designs in reliability, manufacturability, and cost-effectiveness, together with a draft Design Requirements Definition for the conductor that represents a sound basis for continued development and proof-testing of subscale conductor elements as well as a full-scale conductor prototype.

3.2 Results of Design and Analysis Effort (Tasks I and II)

The results of the design and analysis effort on magnet and conductor are described in more detail below:

3.2.1 Magnet Preconceptual Design

The magnet design was reviewed and developed in more detail. The design included some of the following elements:

Clamp Plates to Support Winding During Assembly

A means of securing the winding to the coil-form during assembly was designed and is illustrated in cross-sectional sketch, Fig. 1. The six quadruple pancakes of each coil are assembled on the coil form and clamped tightly to it by the clamp plates and side plates shown. The plates prevent the pancakes of the first winding-half assembled from dropping away when the coil-form is rotated 180° in preparation for assembly of the second winding-half. After both winding-halves are in place and secured by clamp and side plates the cover plates (part of the main longitudinal structure) are installed and then the beams

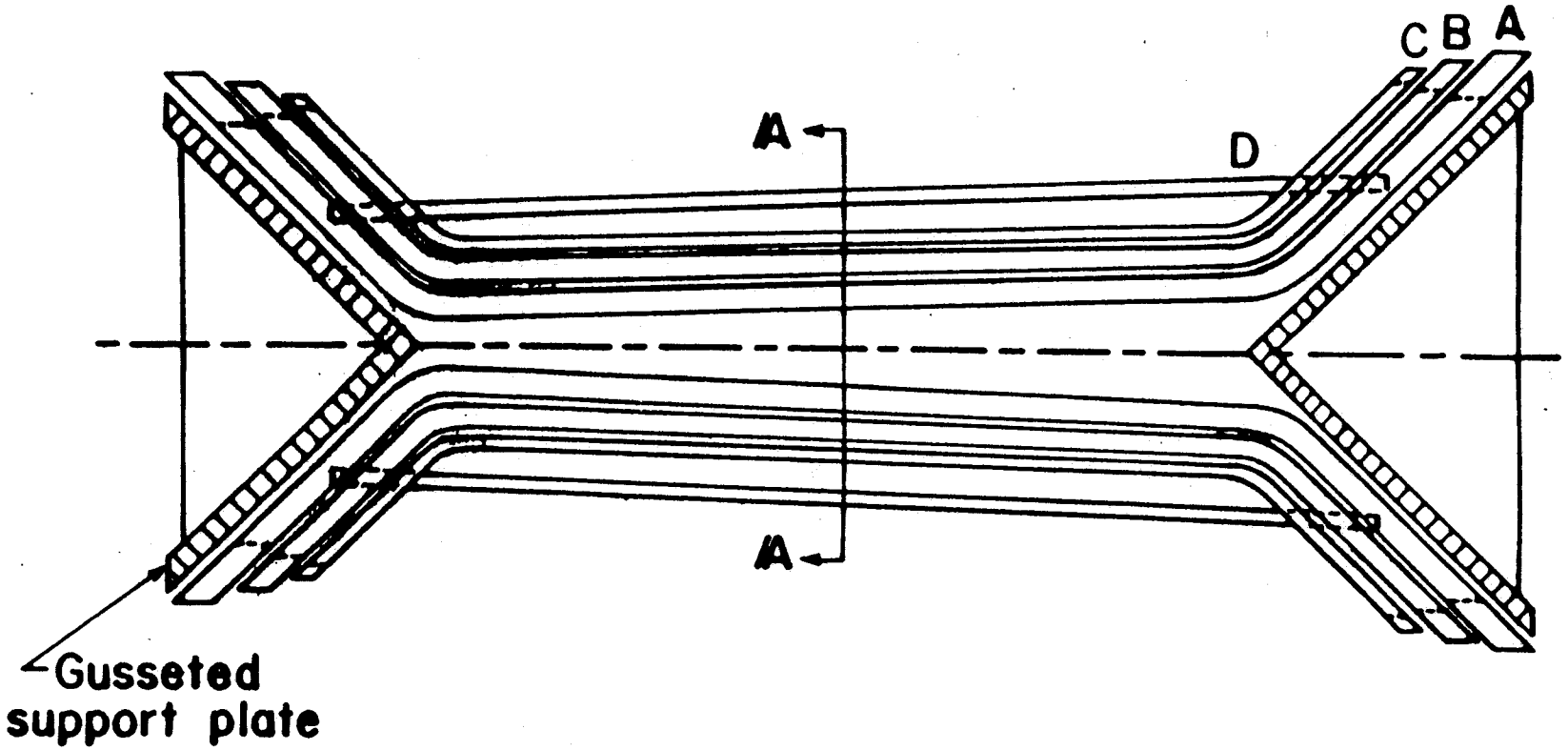

Figure 1: Sketch, Cross Section of Magnet Winding and Support Structure in Straight Portion

and tension rods (which constitute the main transverse structure). The cover plates, beams and tension rods are shown in phantom in Fig. 1.

Cooling Plates to Reduce Heat Leakage into Winding

A means of reducing heat leakage into the windings was designed and is also shown in Fig. 1. This consists of a copper cooling plate interposed between the coil and the coil-form and cooled by helium tracer tubes. The plate will intercept heat that would otherwise flow from the coil-form into the windings and, therefore, reduce the amount of coolant flow required in the conductor itself during steady-state operation. Lowering the coolant flow in the conductor is beneficial because it reduces pumping losses. This feature is conceptual and requires further investigation to verify thickness of plate, and other technical detail.

Arrangement for Leads and Splices

An arrangement for bringing out leads from each quadruple pancake, for separately cooling splices and for making helium connections, was designed and is illustrated in sketch, Fig. 2. In the end-turn region shown, the winding is curved in a circular arc in the portion between the 60° riser bundle and the crossover bundle. These curved portions are self-supporting against outward-acting magnetic forces. Supporting structure is not provided at either the outer or inner surface of these bends. Therefore, the bend regions are at a convenient place to make electrical and coolant connections. Each quadruple pancake is made of a single length of internally cooled cabled conductor, with ends extending well beyond the pancake (3 to 4 meter extensions). Coolant connections are installed in the cable at the three internal pancake-to-pancake transitions, located so that they are accessible at inside and outside of a bend. The bend selected for connections is that bend which is located at the top of the magnet at the exit end. A single large stack is located at the top of the magnet at the exit end above the winding end-turns. The extended cable-ends (leads) from each quadruple pancake are brought out at the open bend, worked back toward top center above the cover plate and main supporting structure and then carried up into the stack and splice-box through insulated feed-throughs. The splice-box is filled with saturated liquid helium at approximately 1.2 atm. pressure, so that the splices are cooled by boiling helium.

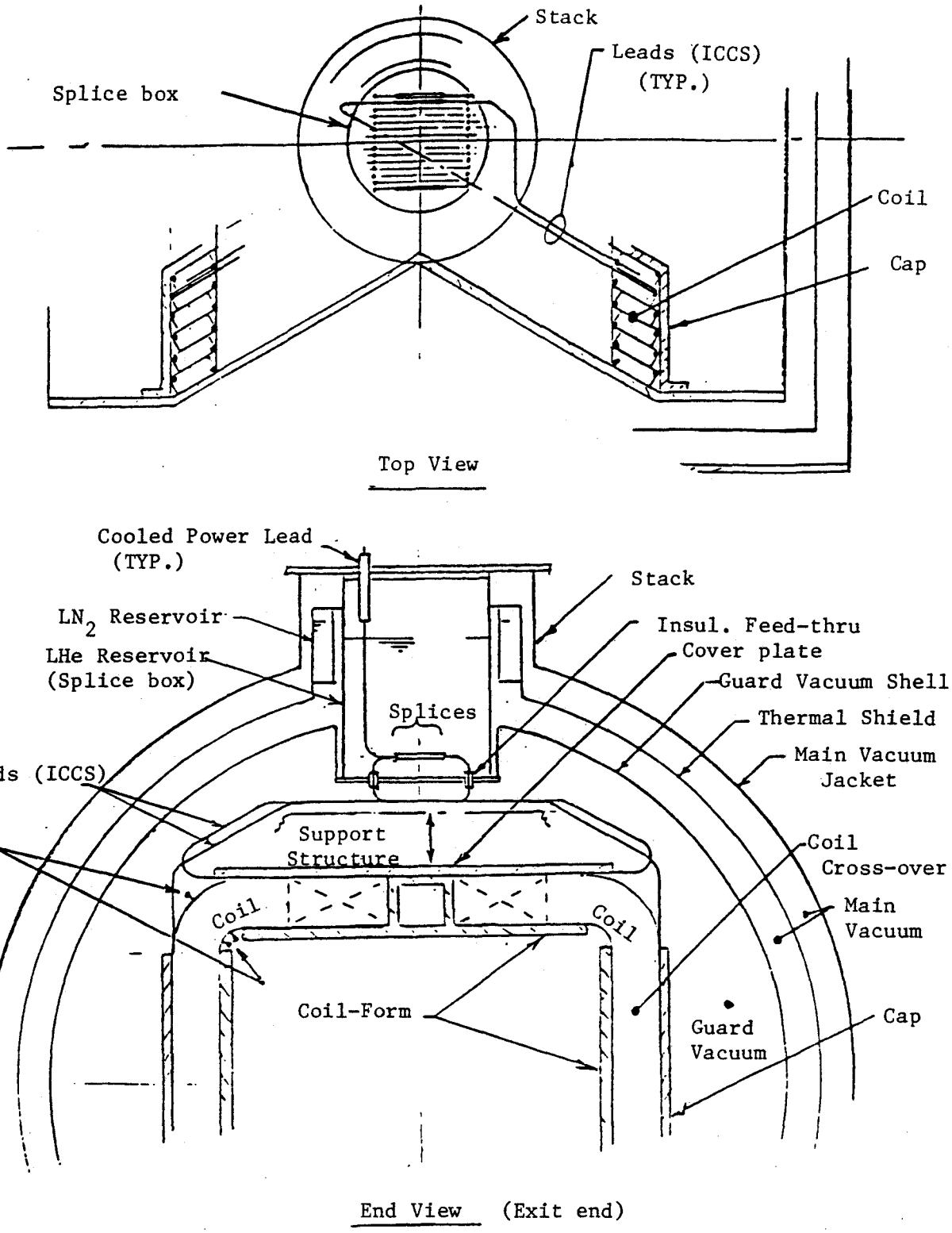

Figure 2: Sketch Showing Arrangement for Leads and Splices in the Region of the End Turns

Weight Estimates

A review was made of magnet weight estimates. Alternative magnet designs had been developed, differing in thickness of plate used in the internal structure (coil-form, cover plates, etc.) and hence having slightly different component and total weights, as listed below:

	Weight (tonnes)	
	Design A	Design B
Conductor	47	47
Insulation	5	5
Coil Form and End Plates	39	52
Cover Plates	12	15
Clamp and Side Plates	9	6
Caps	6	7
Beams and Tension Rods	53	53
Guard Vacuum Shell	24	32
Other (cold stack, et c)	10	10
Thermal Shield	15	15
Vacuum Jacket	100	100
Magnet Total	**320**	**342**

These weights were found to be consistent with design characteristics. It should be noted that the total magnet weight of 320 tonnes listed in Reference 2, is in accordance with Design A above. It should also be noted that the design stresses in longitudinal structure, listed in the Analysis Report, Reference 3 are consistent with Design B.

Choice Between Alternative Designs

A further review of the design of the core-tube and associated structure indicated that the strength of these components in Design A is adequate. That design is preferred because of its lower total weight. A discussion of longitudinal stresses in the core-tube and associated structural members appears below.

3.2.2 Analysis

Magnet system and conductor analyses that were performed in the preceding period were reviewed, including electromagnetic analysis, thermodynamic analysis and structural analysis.

Maximum Field in Winding

The determination of maximum field in the winding was rechecked by several alternative methods, because it is a critical factor in the overall design. Detailed three-dimensional computer calculations on the chosen design indicated a maximum field in the winding of 6.92 T.

Inductance and Stored Energy

The inductance and stored energy were calculated using the method described on page 105 of Reference 4. Entering ratios α and β (1.42 and 0.96) in the curves shown in Fig. 2.102 of Reference 4, the normalized inductance, $L/(\mu_o \ell N^2)$ is found to be 0.52. Taking number of turns, N = 672, ℓ = 10.3 m and $\mu_o = 4\pi \times 10^{-7}$ we determine that inductance, L = 0.515 $\mu_o \ell N^2$ = 3.009 henries. Taking design current, I = 18,000 A, we determine that stored magnetic energy, E = 0.5 LI^2 = 487 MJ.

Stress in Longitudinal Structure

The structural design and stress in the coil-form and associated longitudinal structural elements were reviewed (see Fig. 6 of Reference 3). Alternative designs examined were similar in configuration but different in wall thickness (cross section in plane of peak on-axis field) as shown below:

Structural Element	Design A		Design B	
	Wall Thickness cm	Section Area cm^2	Wall Thickness cm	Section Area cm^2
Coil Form	3.81	2419	6.35	4031
Cover plates	3.18	1129	3.81	1355
Guard Vacuum Shell	1.91	2642	1.27	1761
Conductor Sheath (672 Conductors)	0.165	922	0.165	922
Total	–	7112	–	8069

With a total longitudinal tension force (x-direction) of 4136 tonnes, the calculated stresses in the structural elements are given below for various assumed load distributions:

	Stress (MPa)	
Assumed Condition	Design A	Design B
Load Distributed on All Elements	56.8	50.1
Load Carried by Coil Form and Guard Vacuum Shell	80.0	69.9
Load Carried by Coil Form Alone	167.3	100.4
Load Carried by Guard Vacuum Shell Only	153.2	229.9

All the above elements are of 304 LN stainless steel operating at 4.5 K, at which temperature the maximum allowable design stress is 414 MPa (see Table II, Reference 3). Therefore, the stresses in the structural elements as listed above are considered conservative.

The coil-form wall thicknesses are greater than would be necessary for tensile loading only, because they are selected to withstand inward pressure loading and bending due to

winding precompression, without being overstressed or deflecting excessively. A simplified analysis to determine approximate behavior of the coil form under external pressure follows.

Assume the coil form is a duct 2.1 m square with walls of uniform thickness externally loaded by 1 atm. pressure (vacuum inside). Bending stress and deflection calculated by simple beam theory are as follows:

	Design A	Design B
Coil Form Thickness (cm)	3.81	6.35
Max. Bending Stress (MPa)	155	56
Max. Deflection (cm)	0.59	0.13

The stresses and deflections shown above are moderate and considered acceptable for Design A and quite conservative for Design B. It has been taken into account that pressure loading could be at room temperature (prior to magnet cooldown) at which condition maximum design stress would be only 184 MPa. However, if winding precompression loading achieved by prestressing the tension rods is added to the 1 atm pressure load, then stresses and deflections would become excessive, particularly in Design A. It was decided that prestressing the winding via the tension rods was not necessary for this type of winding. Another means of preloading, such as a midspan beam-to-coil-form tie-rod could be employed. Therefore, it was considered that Design A was adequate. This matter should be investigated further if this preconceptual design is carried into a future (prototype) design stage, rather than the revised design presented below (section 3.4).

Pressure Drop and Friction Heating in Coolant Circuit

Pressure drop and friction heating in the coolant circuit of the windings were reviewed. The flow diagram, Fig. 3, shows coolant flow rates, temperatures and pressures in the magnet winding. Pressure drop and pumping power are calculated as follows:

Conductor length, L, single pancake	(maximum)408 m
Mass flow rate	1 g/s
Density, p, at 3.2 atm, 4.5 K	0.13 g/cm^3
Volume flow rate, ν	7.7 cm^3/s
Conductor void area	0.89 cm^2
Flow velocity, V	8.65 cm/s
Reynolds number, R_e	1500
Friction factor:	
$f = \frac{12.7}{R_e} + \frac{0.0698}{R_e^{0.25}} + 0.0146 = 0.0343$	

Assume 25 W enter the winding through conduction and radiation from surroundings.

Total heat into winding - 50 W

Total flow rate through winding - 48 g/s

Heat flow into coolant = $\frac{50}{48} = 1.04$ J/g

Temperature rise of coolant $\cong$ 0.1 K

Exit pressure of coolant $\cong$ 2.5 atm

The results of the calculations shown above indicate that pressure drop and friction heating in the preconceptual design magnet winding will be within reasonable limits, provided the heat leakage into the winding from the surroundings remains at or below the (conservatively estimated) level of 25 W.

3.3 Revised Conceptual Design for Retrofit Magnet System

After analysis of the original subscale conductors, it was determined that a revised magnet design would incorporate the new conductor more successfully than the original design described above. Several system design iterations were carried out, the result being a well-defined double pancake configuration that incorporates a conductor that itself has undergone several design iterations.

With this latest iterative generation of conductor and pancake design in hand, a computer stick model was finalized, and a complete set of field and force calculations was carried out. From the tabulated and graphic output of those calculations, the axial field profile, the maximum field at the conductor, the forces on the individual subcoils, and the field profile within the MHD channel have been determined.

3.3.1 Description of Conductor and Pancakes

The cable is wound of 60 strands of NbTi superconductive wire, 0.076 cm in diameter, with a Cu/sc ratio of 1.35:1, and encased in a sheath of high-strength aluminum. The sheath measures 2.18 cm $\times$ 2.18 cm, with 0.3 cm outside corner radii. The cable is contained within the circular bore which measures 0.73 cm in diameter. Figure 4 shows the conductor in a double pancake configuration, with an insulation wrap 0.08 cm thick and a pancake insulation also 0.08 cm thick. The total thickness of each double pancake is 5.0 cm.

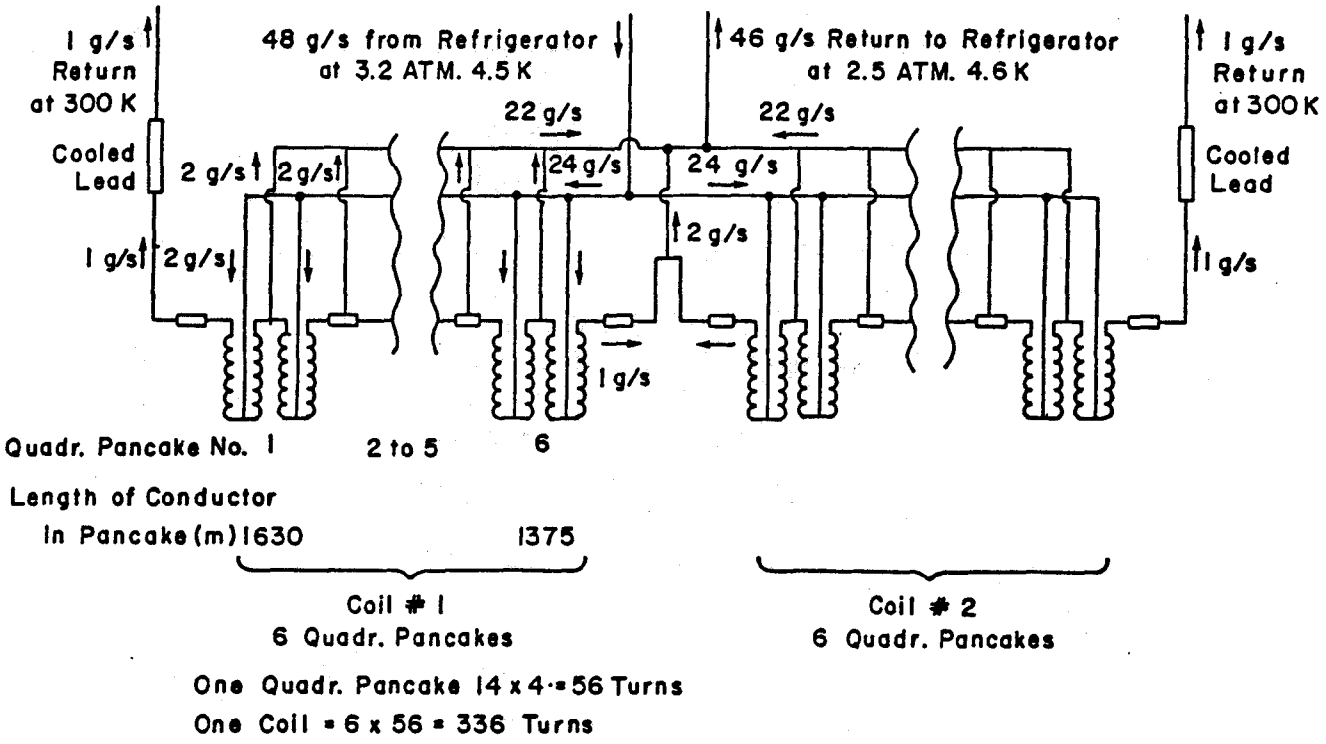

Figure 3: Electrical and Coolant Flow Diagram, Magnet Winding

Table 3.3-1
Conductor and Double Pancake Characteristics

Void Fraction	0.35
Cross section of strands (cm^2)	0.272
Helium space (cm^2)	0.147
Total cable space (cm^2)	0.419
Conduit section (cm^2)	4.256
Hydraulic diameter (cm)	0.04
I_c, 5.5 T, 4.2 K (kA)	20.4
I_{op} (kA)	12.87
T_{op} (K)	4.5
T_{cs} (K)	5.26
T_c, 5.5 T (K)	6.6
I_{op}/I_c	0.63

The mass per unit length of conductor, exclusive of the insulation wrap, is tabulated next:

Table 3.3-2
Mass per Unit Length of Conductor

Strands	0.2437 kg/m
Aluminum	1.15 kg/m
Helium	0.002 kg/m
Total	1.4 kg/m

Subcoil Layout

The coil system comprises two sets of four subcoils mounted on either side of the MHD channel. Figures 5 and 6 show the relative sizes and locations of these coils in the first quadrant of the device coordinate system at the channel inlet and outlet respectively. Subcoil D is a racetrack coil (no saddle ends) which extends through the saddles of subcoils A, B and C. It serves both to improve field uniformity and to reduce the peak fields in the winding, which occur at the insides of the saddles. The peak field in this new design has been reduced to 5.53 T. Table 3.3-3 lists the subcoil characteristics.

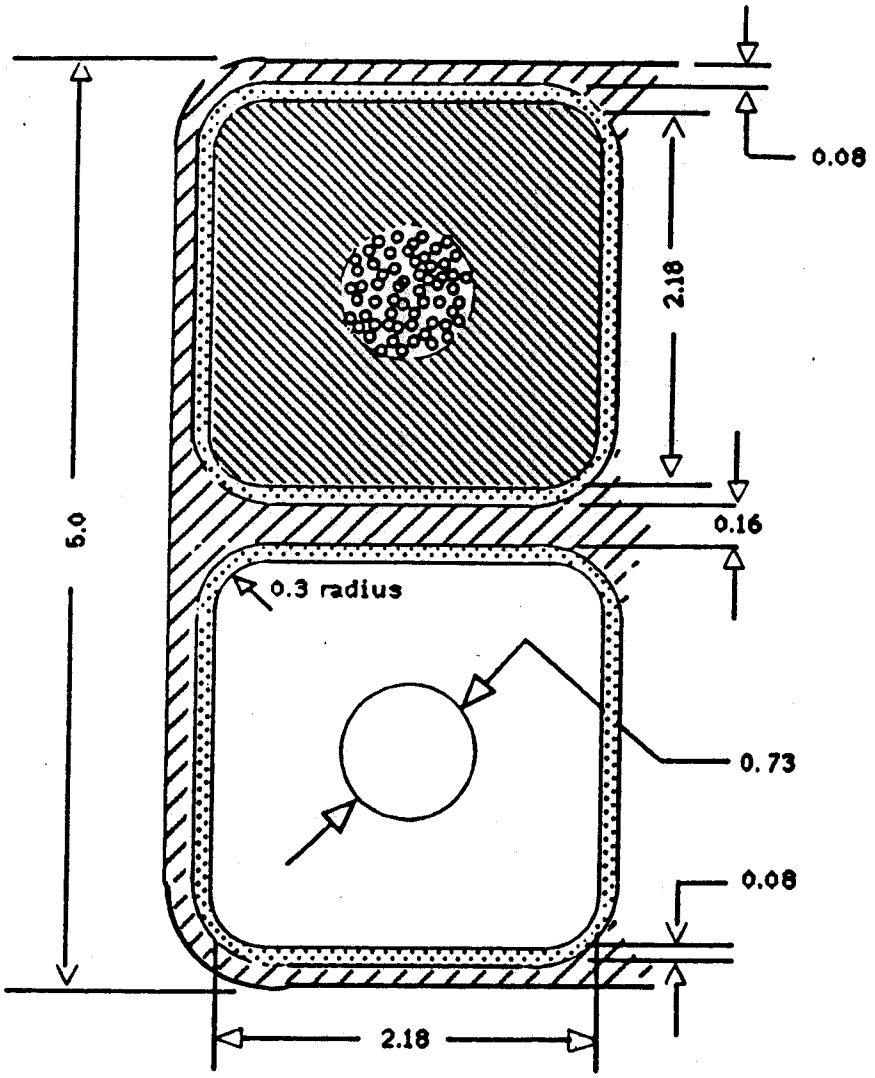

Figure 4
Double Pancake Configuration
(all dimensions in cm)

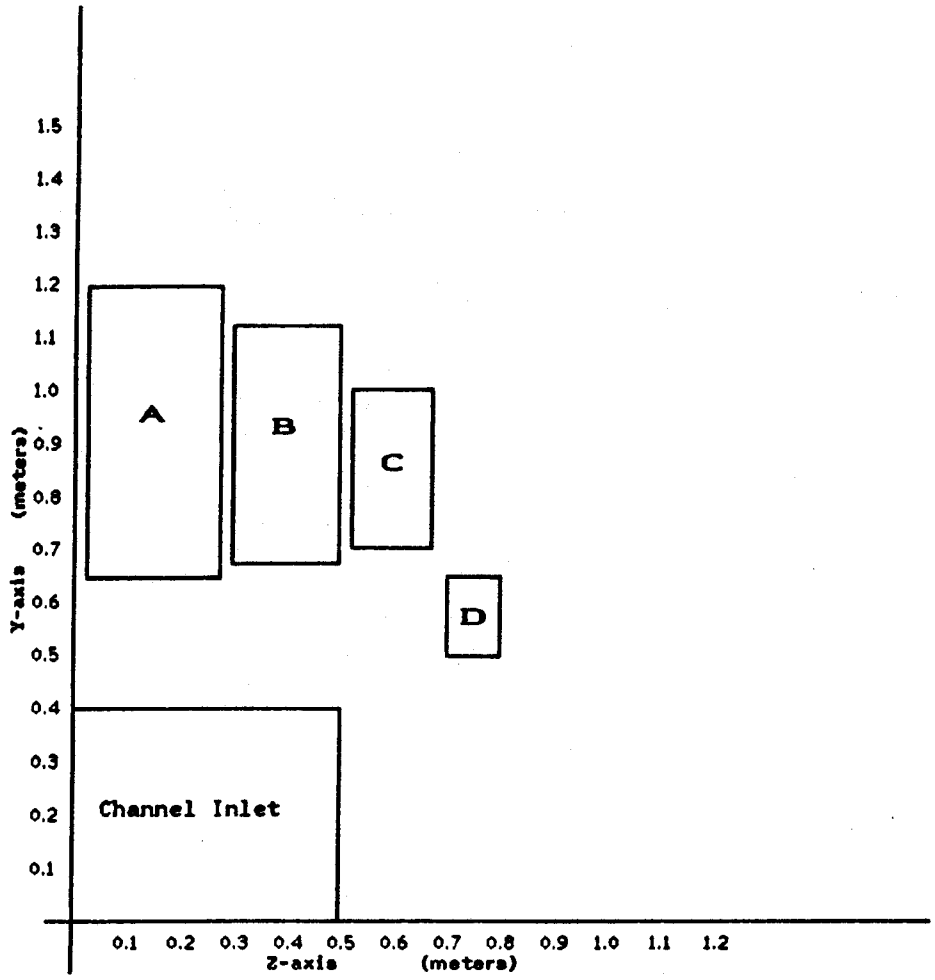

Figure 5
Winding Block Distribution at Channel Inlet

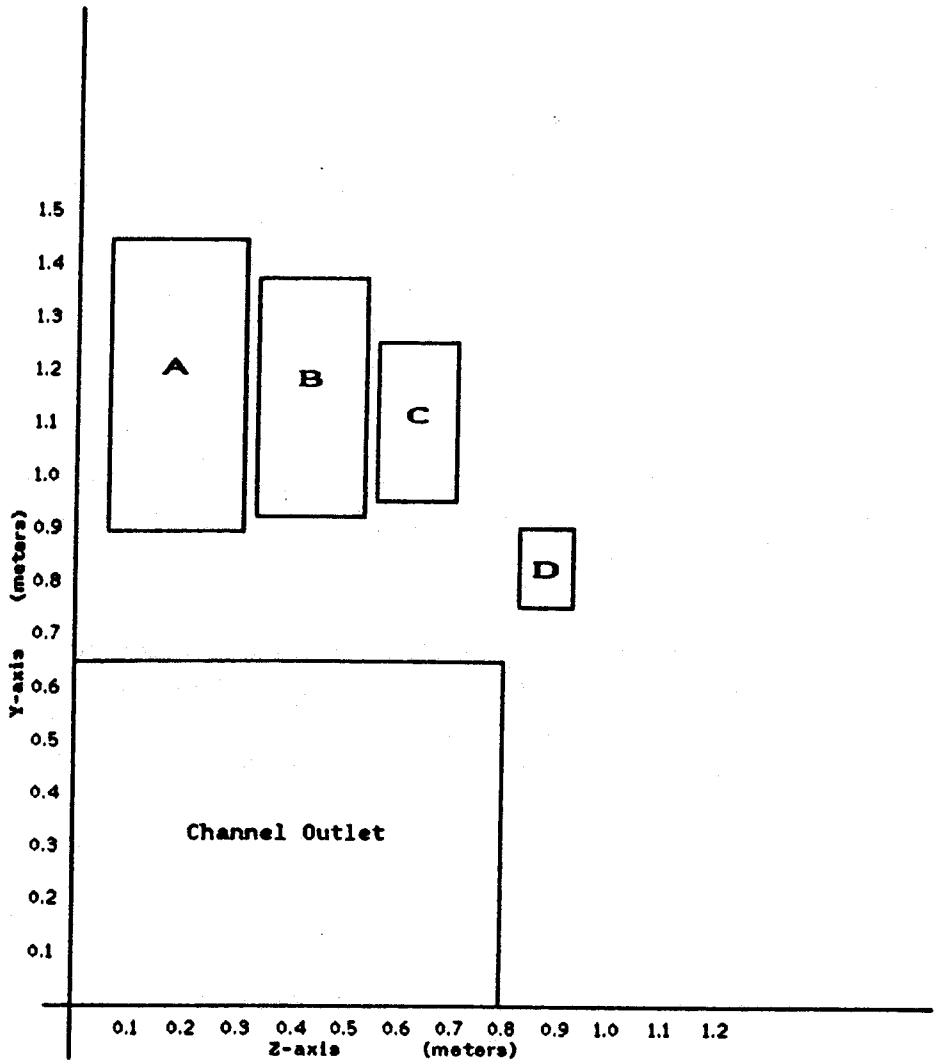

Figure 6
Winding Block Distribution at Channel Outlet

Table 3.3-3
Subcoil Characteristics

	A	B	C	D
Build (turns)	22	18	12	6
Number of Dbl. Pancakes	5	4	3	2
Dimensions (m)	0.5164 x 0.25	0.4228 x 0.2	0.2824 x 0.15	0.1424 x 0.1
Cross section (m^2)	0.129	0.0846	0.424	0.142
N (turns)	220	144	72	24
NI (MA-turns)	2.8318	1.8536	0.9268	0.3089
Overall J_c (A/cm^2)	2193	2192	2188	2175

Manufacturing Considerations

The goal of minimizing the cost of manufacturing this conductor has led us to begin the decision-making process by first imagining the most desirable means, e.g., the process with the fewest manufacturing stages, and then working from that concept toward some plausible compromise between desirability and feasibility.

Cabling of 60 strands of superconductive wire will not present any difficulties, nor will wrapping the cable with a thermal barrier, if that is desired. The greatest challenge will be encapsulating the cable within the aluminum sheath; the most desirable process (minimum number of steps) would be to co-extrude the aluminum over the cable. This has been done by at least one European manufacturer,[8-9] but whether it could be done with our configuration, with the high-strength alloy that we require, and in the long lengths that we require is a topic for further investigation. If co-extrusion proves to be infeasible, other fabrication means will be explored.

3.3.2 Calculations Based Upon A Multistick Model

The stick model treats all four subcoils in the same way, with clusters of four conductors being represented by one filament. Each filament is made of sixteen straight segments. Coil A comprises 55 filaments, coil B, 36 filaments, coil C, 18 filaments, and coil D, 6 filaments. Thus, with two coil sets—one on either side of the channel—each made up of four subcoils, the total number of sticks in the model is 3680.

The following table gives the total length of conductor, calculated on the basis of the filament model; the actual length of conductor that would be needed to wind these coils would be slightly larger, because the actual saddles would be circular or elliptical in shape rather than five straight sections as depicted. The total mass listed in the table also is based on the stick model.

Table 3.3-4
Length and Mass of Conductor in Subcoils

	A	B	C	D
total length (m)	12705	7755	3631	1122
mass (kg)	1772	1082	506	157

Fields and Forces at the Windings

Several forms of graphic output were devised in order to enhance the insight that the designer could garner from the model-based calculations. The computation of fields and forces at stick midpoints produced prodigious quantities of output that were best digested in graphic format rather than as tables of numbers. A sample plot is shown as Figure 7. Numeric data given in the tables were generated by appropriate summations of the stick model data.

With the value of current selected (12.87 kA) to yield a peak on-axis field strength of 4.5 T, the calculated maximum field at the winding was found to be in subcoil B, at the point where the inlet saddle bends to become a long straight section: this maximum value was 5.527 T in this revised design. The next highest value was found to be in subcoil C, where the outlet saddle transition is located; this value was 5.503 T.

Field Homogeneity

The field strength was calculated over one quadrant of the channel volume on a 5 cm x 5 cm grid for five values of the axial coordinate, and contours of the resulting values were normalized to the value on the axis at each location. The boundaries of the channel wall, and of the plasma cross section, taken to be about 25% of the the channel section, have been outlined to aid interpretation of the contours.

At the inlet ($X = 0$), the homogeneity is better than $\pm 2\%$. At the position of maximum axial field, $X = 1$, it is about +2.5%, -3.5%. Of the points considered, the worst homogeneity was at $X = 8$, where it was +4.5%, -5.5%.

3.4 Conductor Development and POC Tests

The conductor design requirements were established[1] and two candidate subscale conductors were identified and their parameters defined. A test plan[4] was developed, subscale conductor for the long-sample tests was ordered and the test rig was designed. Preliminary conductor bending tests were performed, a test heater was acquired and a number of preliminary tests were performed on it. These included bending tests, soldering tests and performance measurements.[5]

Analytical work on the subscale conductors continued in parallel, with a particular emphasis on stability predictions.

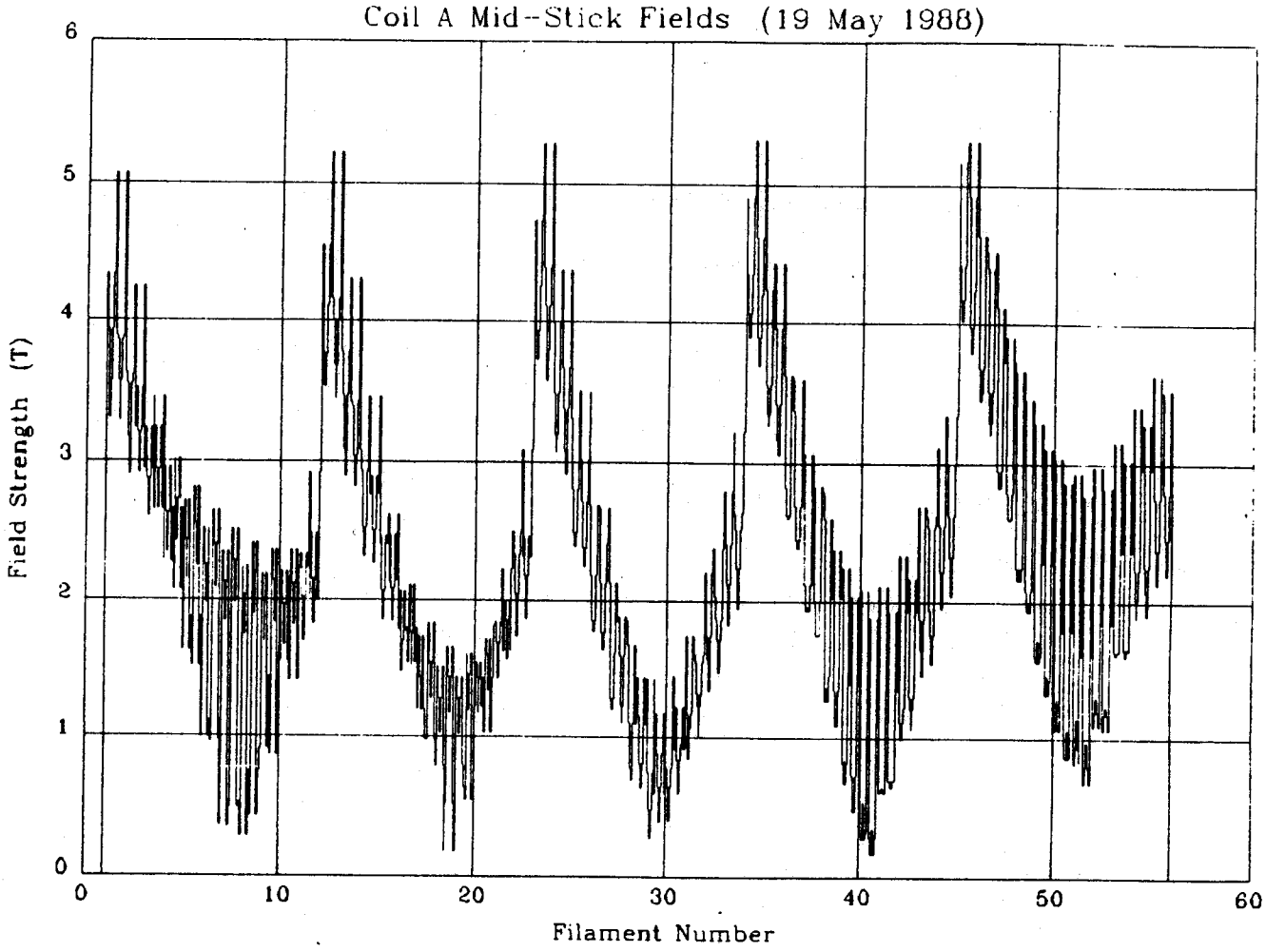

Figure 7
A Sample Plot Obtained with Multistick Model

3.4.1 Summary of Subscale Tests of Separated Copper Conductor

The test rig design, construction and assembly were completed in late 1987. Test parameters were solidified and instrumentation specifications and signal sources decided. Instrumentation leads were attached to the test rig assembly which was then mounted on an experimental probe assembly to allow it to be inserted in a background-field-providing magnet system and to be helium cooled.

Tests were run, data were collected using a LeCroy 32-channel digitizer, and stored on a MicroVax; the data were subsequently analysed. The data indicated that further consideration of the two-in-one copper/superconductor cable configuration might be warranted at some future time. We believe that this conductor will be considerably less expensive to manufacture than the all-multifilamentary copper-superconductor ICCS used as the alternative subscale conductor. Details of the tests and of the results are presented in PFC/RR-88-1.

3.4.2 Tests of POC Conductor With and Without Insulating Barriers

Figure 8 is a photomicrograph of the POC conductor. Two test samples were prepared by winding single-layer noninductive coils on mandrels of G-10, on the OD of which had been machined two V-grooves in a double helix pattern. Figures 9 — 12 show details of the component parts of the coil forms. The total length of subscale ICCS on each sample was approximately 9.2 meters; of this length, approximately 1 m was incorporated into the two end termination assemblies. Every reasonable effort was made to ensure that the sample coils would be physically, electrically, and thermally identical, save for the one difference that was the prime object of the performance comparison, the braided dacron sleeve that insulated the cable from the conduit in one of the samples. Hereinafter, this sample will be referred to as the sleeved conductor, to distinguish it from the conventional ICCS sample, in which the cable is not insulated from the ID of its conduit.

A resistive heater measuring 0.001 m in diameter and 0.3 m in length was soldered with a generous fillet along the outer surface of the conduit at one end of each sample coil. The heater is made so that compacted ceramic powder electrically isolates the internal resistance elements from the heater's stainless steel jacket, thereby permitting the user to solder the stainless jacket directly to the sample with no need to interpose an insulating barrier.

Two experimental runs were carried out, one for each of the test coils. Figure 13 shows the position of the sample coil in the experimental dewar relative to the 10 kA gas-cooled lead assembly. Liquid helium filled the dewar to a level just below the vapor inlets of the lead assembly. Each coil was instrumented with five voltage tap pairs. During each experimental run, a pressure transducer was connected at the sample termination that was nearest the heater. Figure 14 is a schematic of these instrumentation connections. Background magnetic field was generated by a 10 MW, 10" bore Bitter solenoid at MIT's Francis Bitter National Magnet Laboratory. Measurements were made at three values of

field, 5, 6, and 7 T. Transport current was supplied to the sample by a 10 kA constant voltage dc power supply.

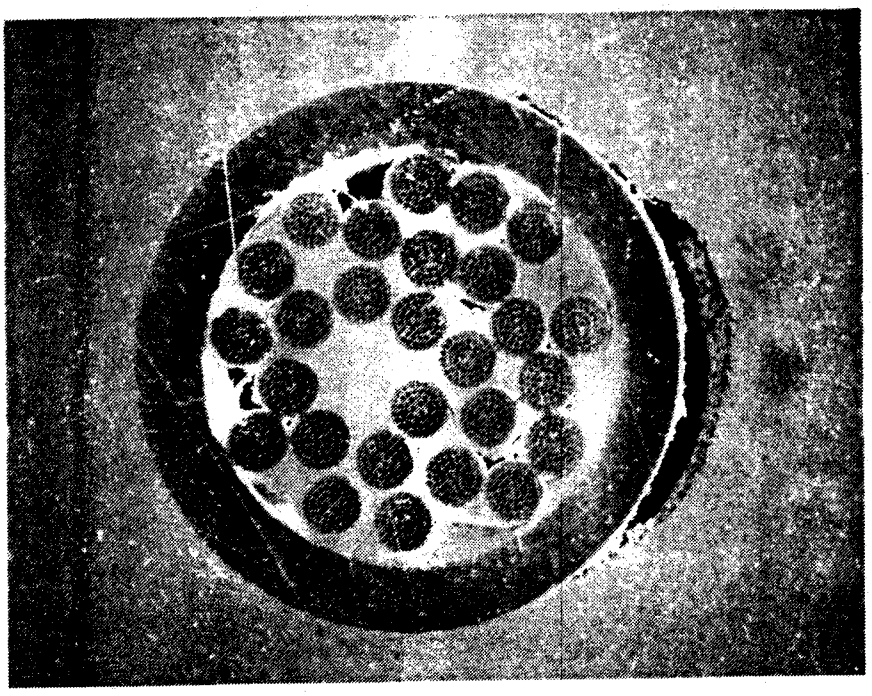

Figure 8
Photomicrograph of POC Conductor
Conduit - DHP Copper; Conduit OD - 0.673 mm; Strands - 27;
Cu:SC of strands - 1.35; Void Fraction - 38%;I_c, kA, @ 7 T - 6.5

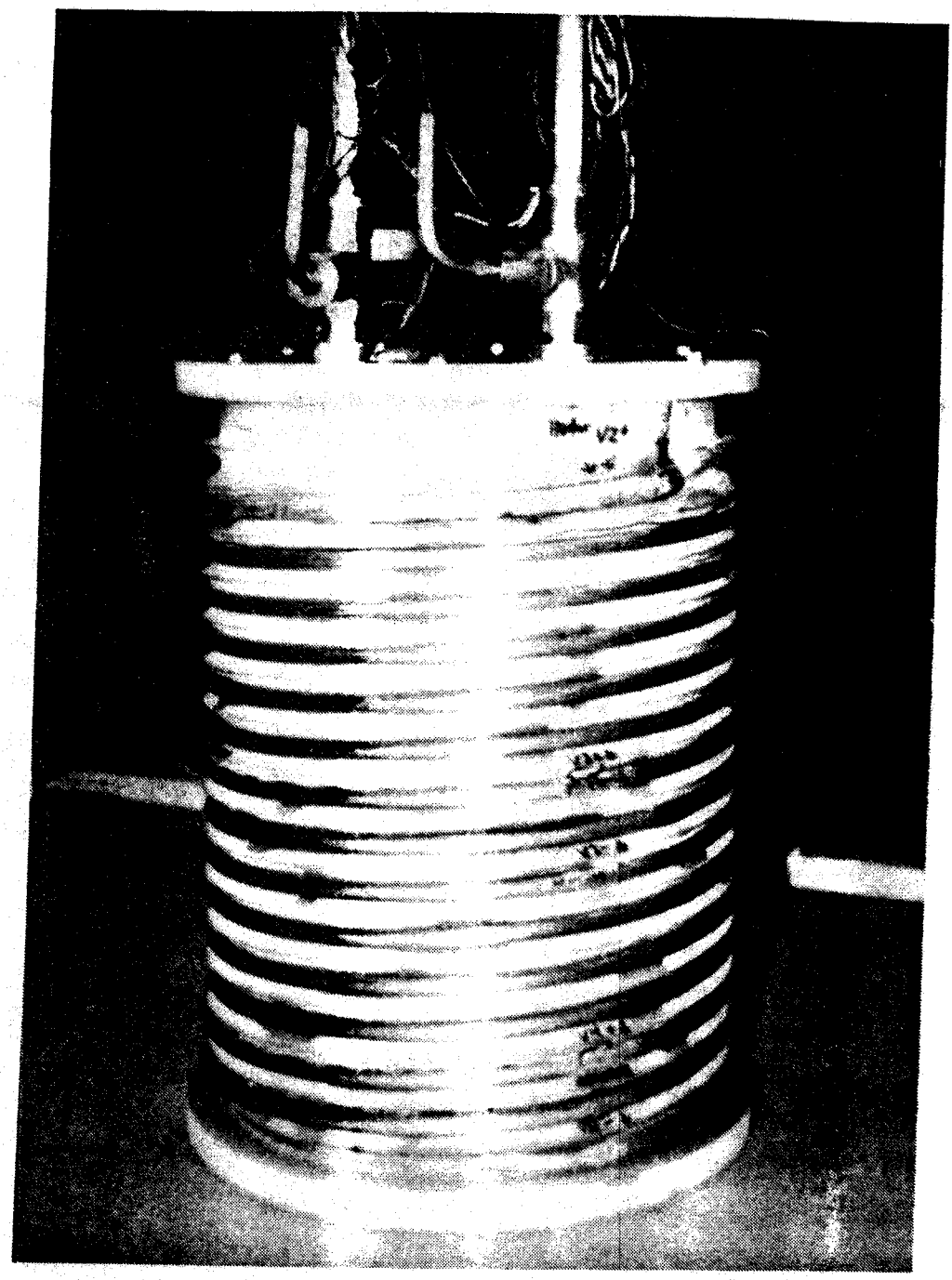

Figure 9
Proof-of-Concept Test Coil Winding

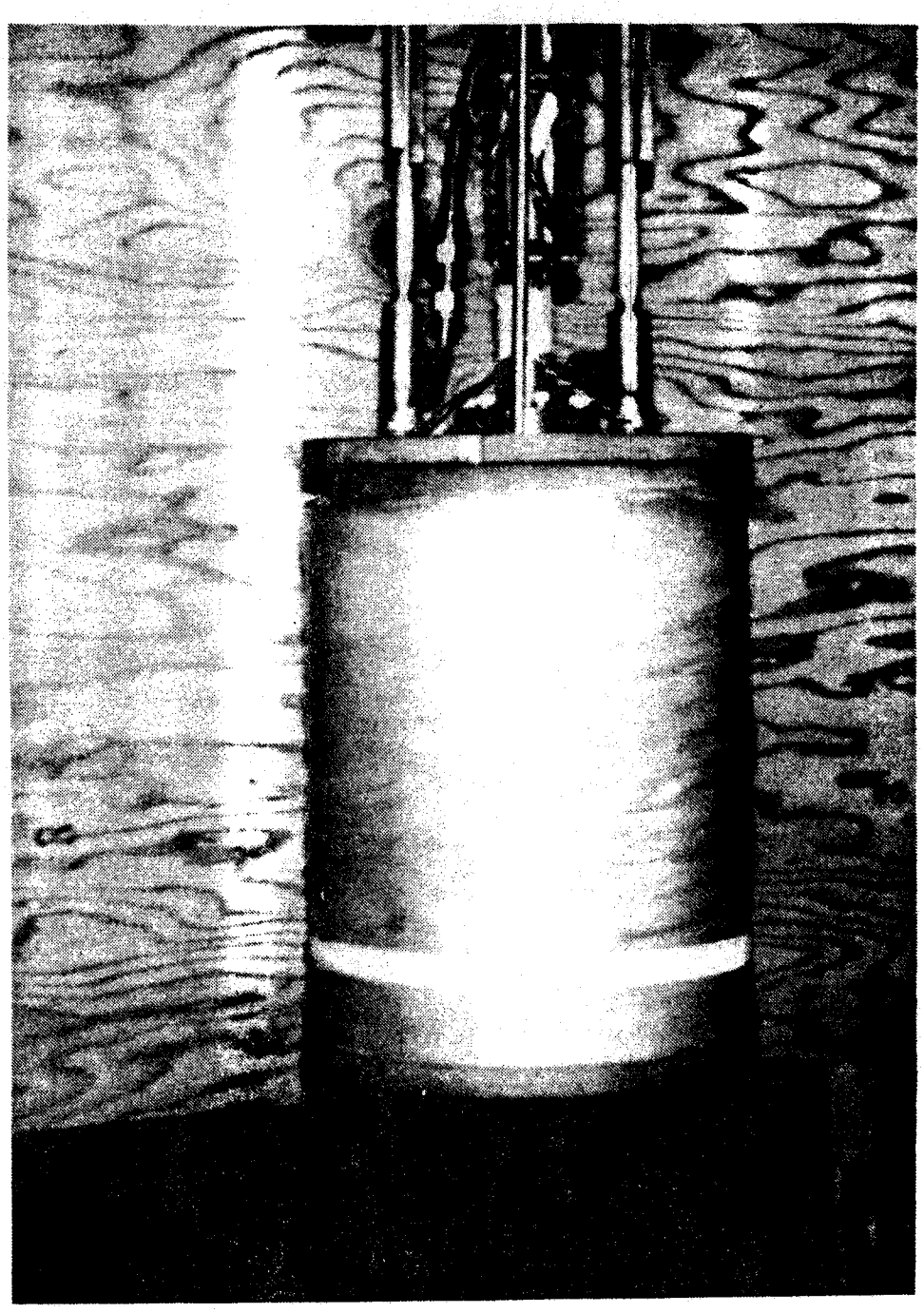

Figure 10
Encapsulated Test Coil

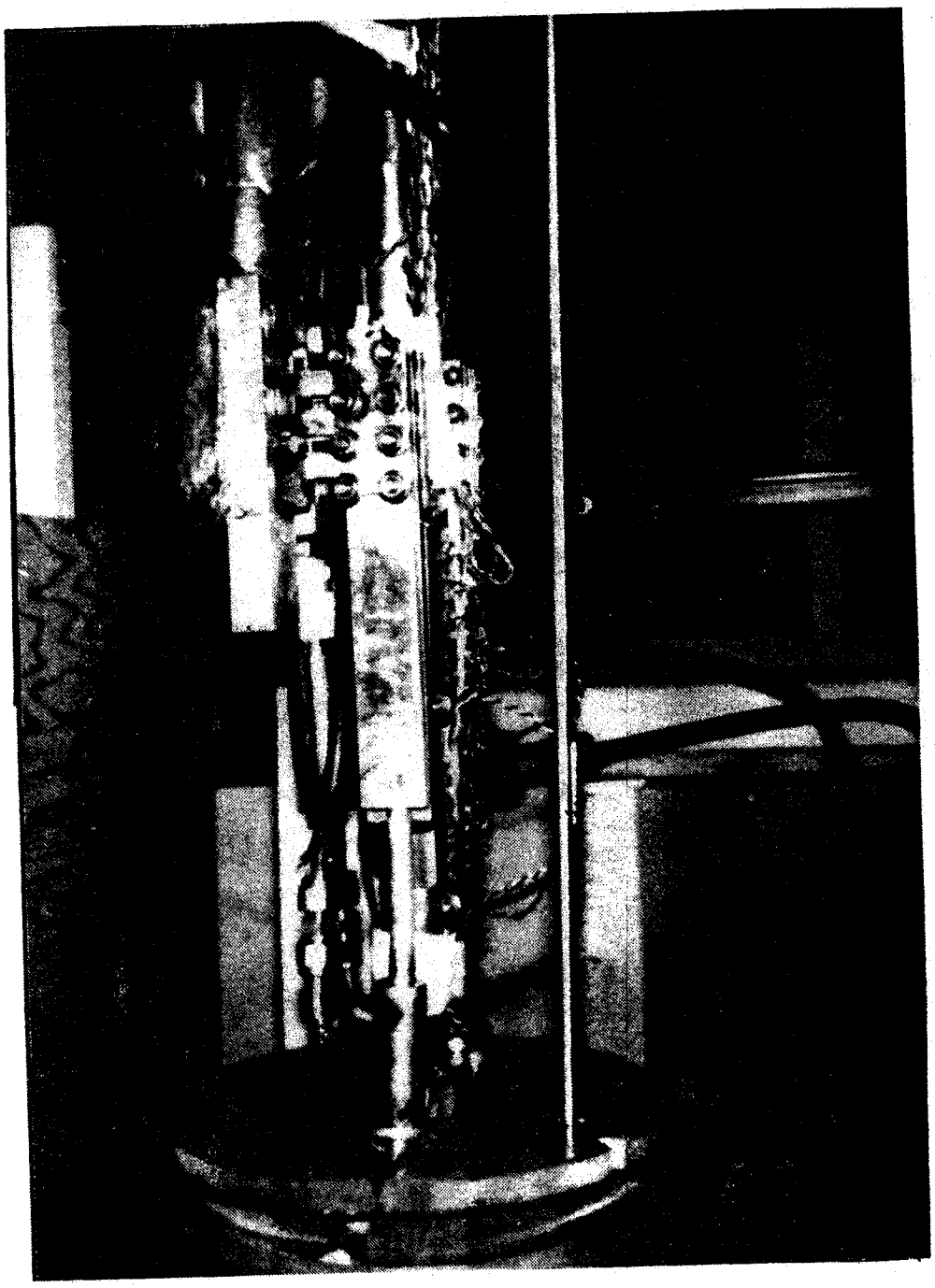

Figure 11
Test Coil Attached to Leads and Mounted, Ready to Test

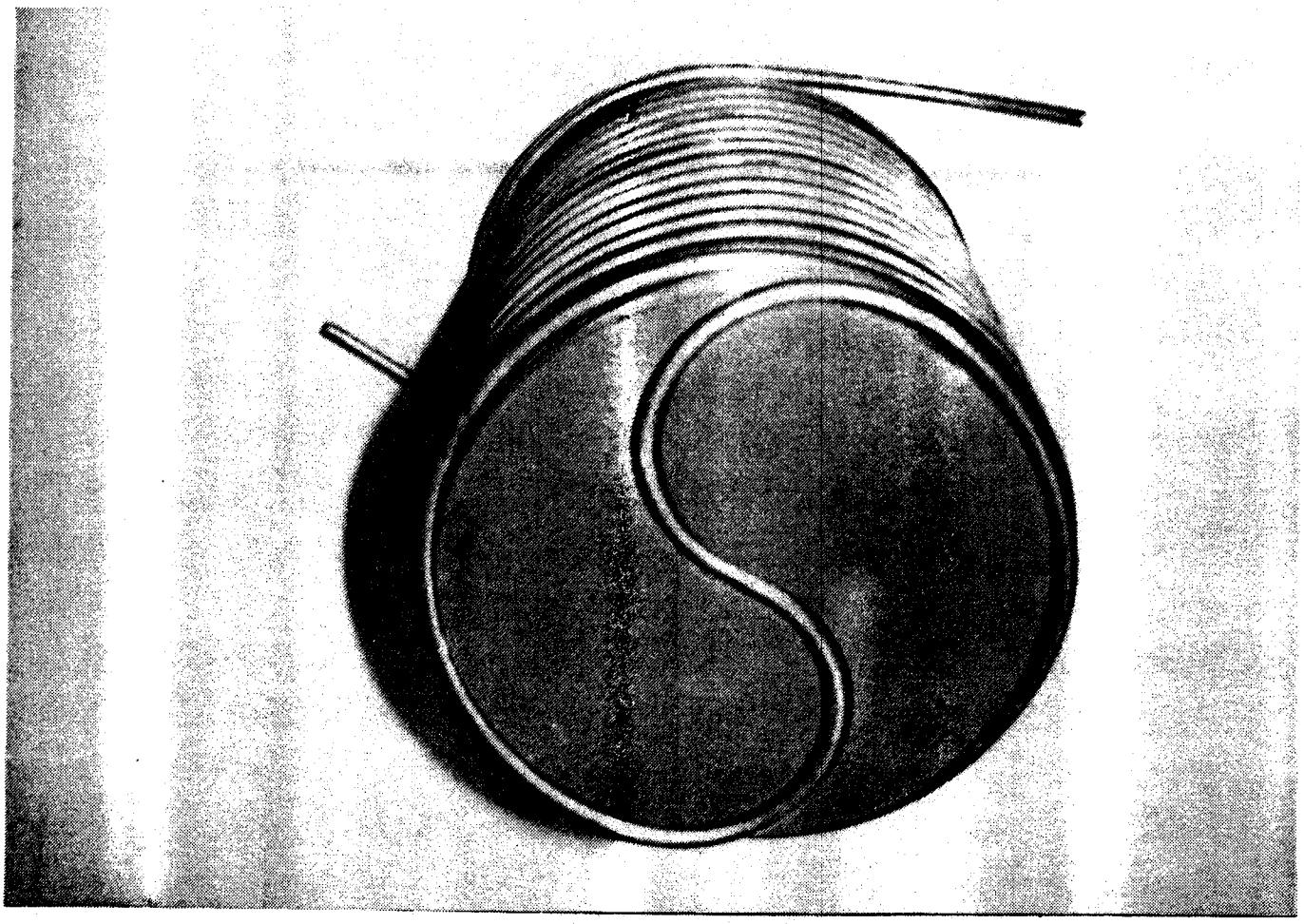

Figure 12
Crossover of Conductor at Coil Base

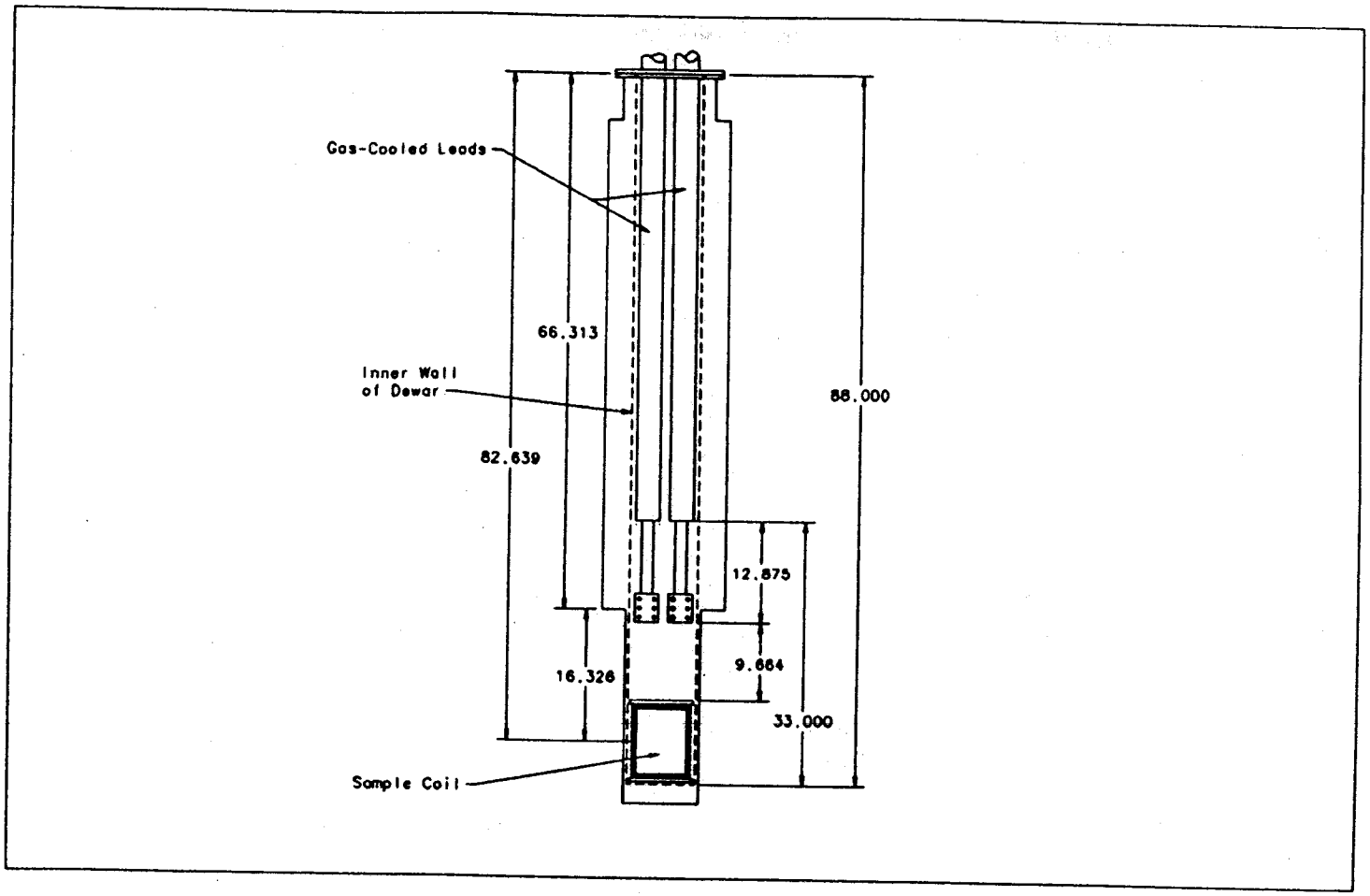

Figure 13
Schematic Illustration Showing Position of Test Coil in Dewar

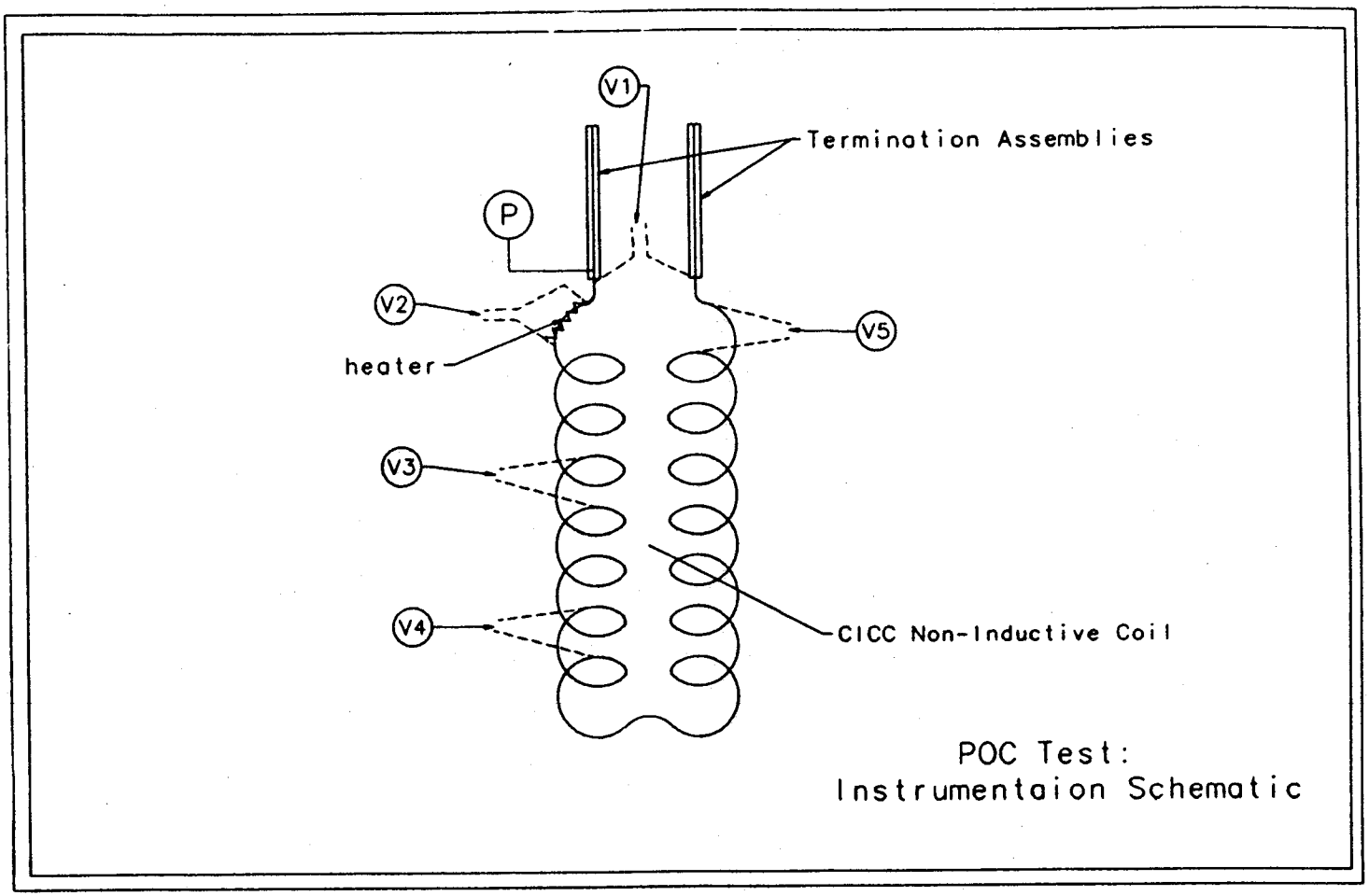

Figure 14
Schematic Diagram Showing Position of Instrumentation on POC Coil

Data acquisition was organized into nine channels, summarized in Table 3.4-1:

Table 3.4-1
Data Acquisition Summary

Channel	Name	Source
1	V1	Coil terminal voltage
2	V2	Voltage across heated length of conduit
3	V3	Voltage across turn 4
4	V4	Voltage across turn 7
5	V5	Voltage across last turn
6	P	Pressure transducer
7	I	Transport current
8	Ih	Heater current
9	Vh	Voltage across heater terminals

The experiment was conducted as follows:

- Current in the background field magnet was set to generate the desired field strength at the conductor;
- the current in the sample was set to a desired value;
- the heater pulse supply (a simple capacitive discharge circuit) was charged to a selected voltage;
- the heater pulse supply was triggered.
- If a propagating normal zone ensued, the transport current supply was interrupted, and the previous steps retraced, but with a smaller heat perturbation.
- If not, the heater was again pulsed with increasingly higher currents until the sample did suffer a nonrecoverable normal zone.

A total of 58 data 'events' were recorded; some were of quenches, some were not.

The amplified raw signals were digitized by 32-channel 12-bit A/D converter, sampling at 2 kHz. The resulting digitized data were read out to a DEC VAXstation II for storage on magnetic disk, and displayed on the workstation monitor. Figure 15 is a schematic diagram of the data acquisition system.

Inasmuch as the dc current source was of constant voltage type, the output current drooped slightly as the resistance of its load—the sample coil—increased during the evolution of a nonrecoverable normal zone. This current decay is readily apparent in the sample raw data plots shown in Figures 16, typical of unsleeved conductor, and 17, typical of the sleeved conductor. These raw curves also show a zero offset in the Pressure channel; in later figures of reduced data, the pressure data is presented as $\Delta P(t) = P(t) - P(0)$.

Even from the raw data curves, one dramatic difference can be seen: voltage traces taken at different locations on the conventional conductor appear sequentially in time, while those on the conductor with the sleeved cable appear essentially all at the same

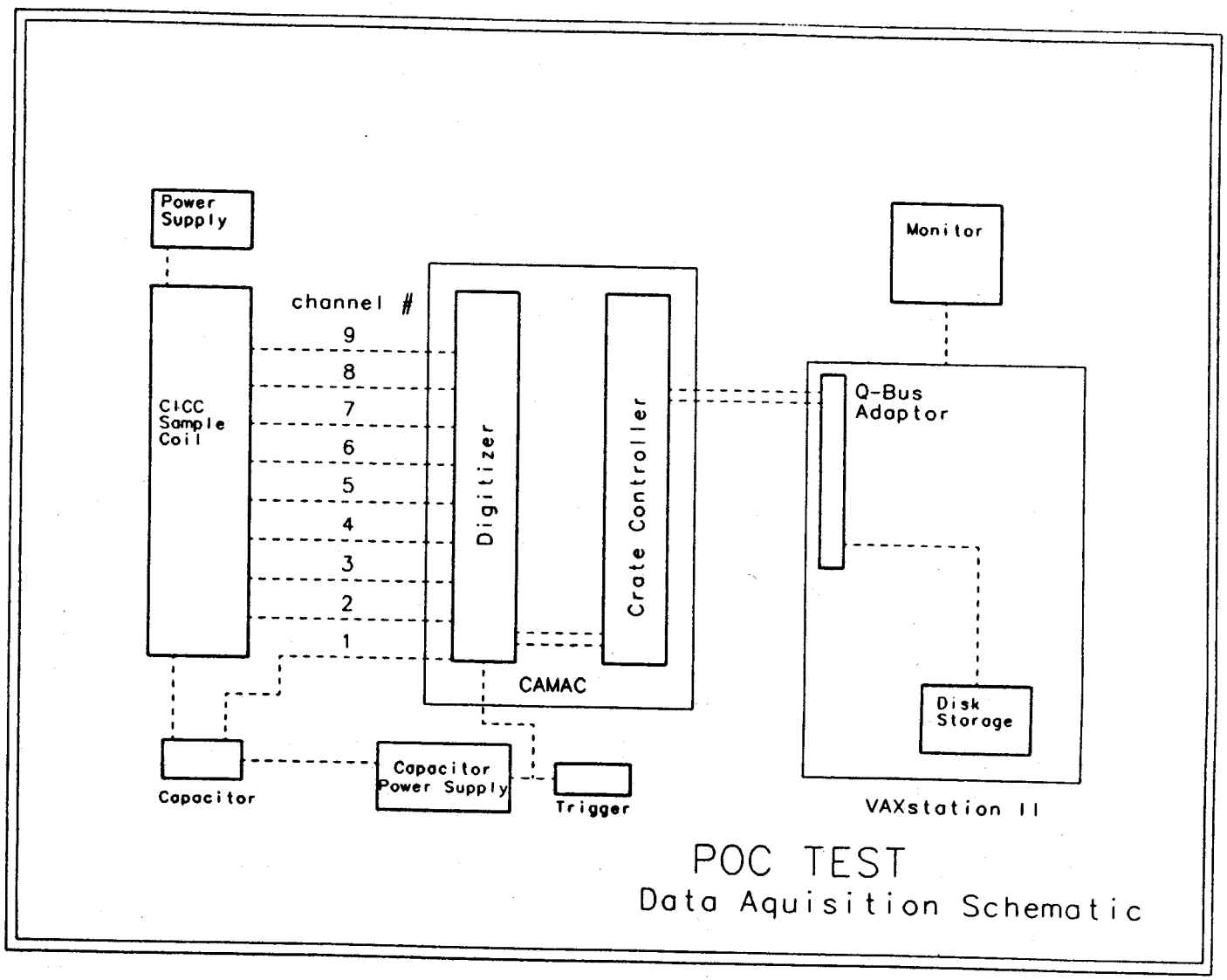

Figure 15
Schematic Illustration of Data Acquisition System

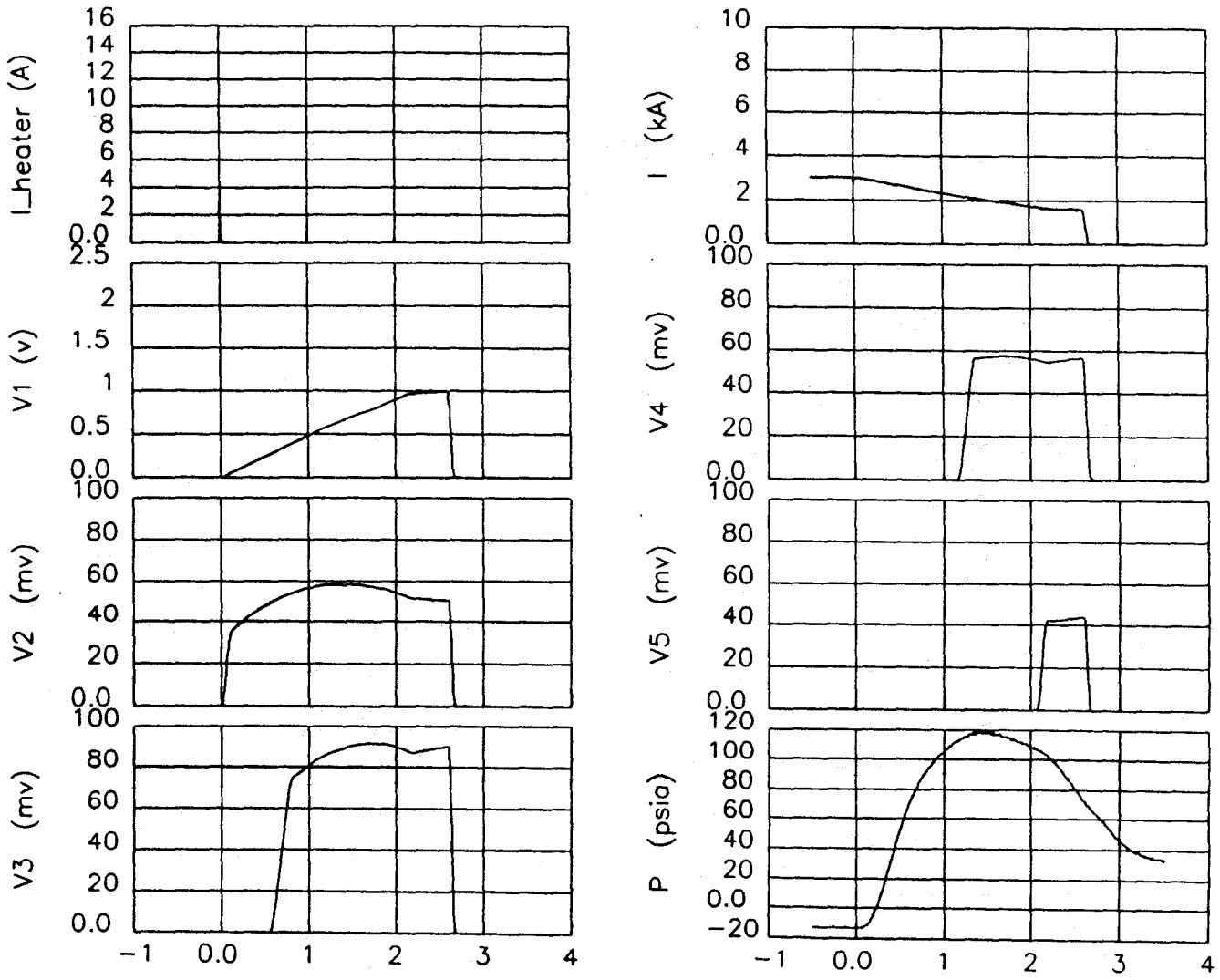

Figure 16
Raw Data – Shot 193. This Conductor had no Sleeve or Barrier

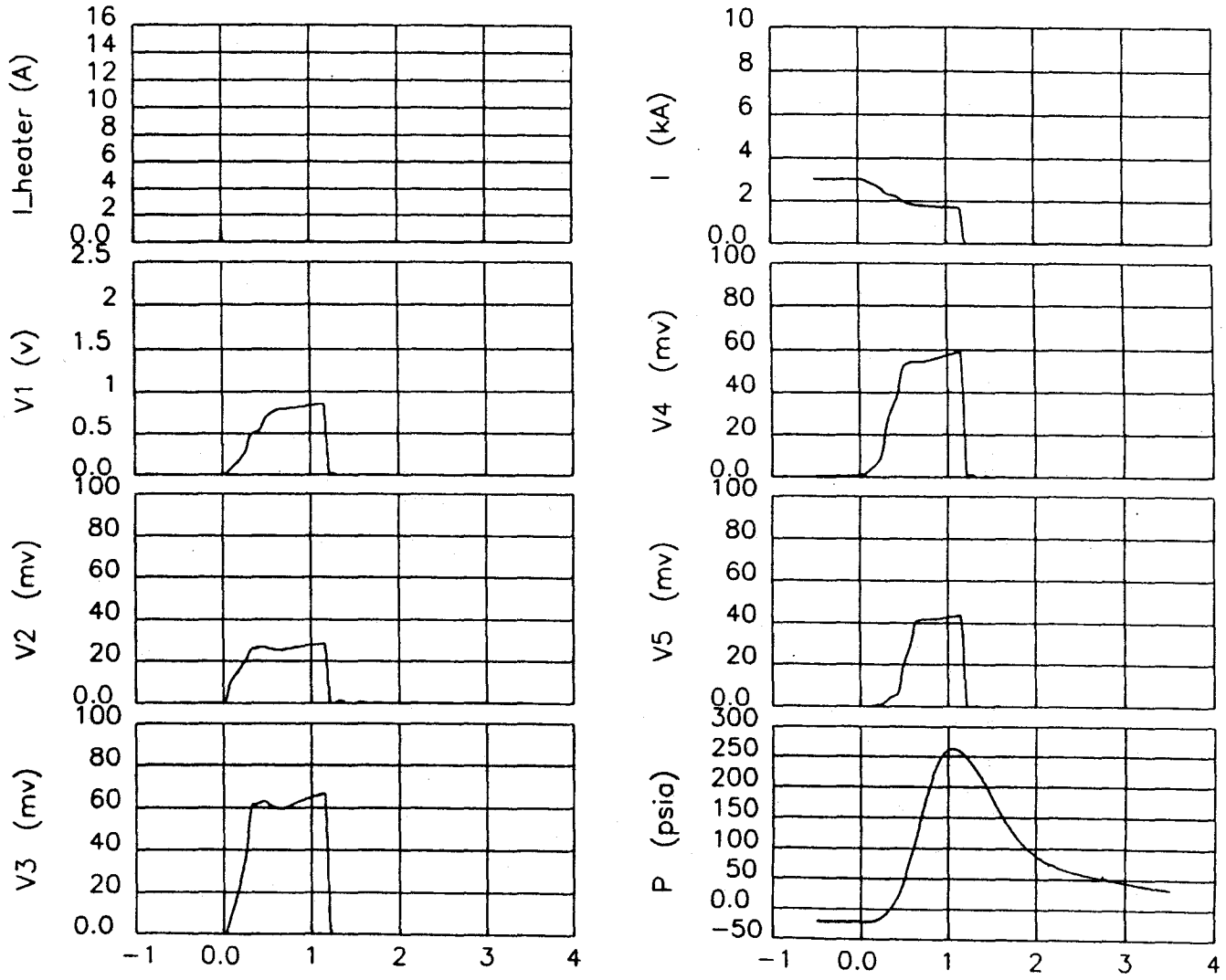

Figure 17
Raw Data – Shot 209. Conductor with Sleeve or Barrier at Same Conditions as in Figure 16

time, at t = 0.

The next six Figures, 18 through 23, are presented here as representative of reduced data, and are useful for making comparisons between the two samples, and between data traces taken under different operating conditions for the same sample. Three of the plots in each figure show the potential drop along the length of conductor spanned by the voltage taps, as a function of time following the onset of the heater pulse (note the expanded time scale in the upper right plot). The fourth shows the trace of the pressure transducer output, relative to the initial pressure. Table 3.4-2 is a summary of the six representative data sets.

Table 3.4-2
Data Acquisition Summary

Shot No.	Sleeved	Background Field (T)	Transport Current (kA)
193	no	7	2.96
209	yes	7	3.00
212	yes	7	3.49
215	yes	6	2.03
240	yes	6	4.50
248	yes	5	4.99

As indicated in the earlier table, the raw potential differences V1—V5 were among the measured parameters. The conductor length for V3, V4, and V5 was one turn, or about 0.56 meter. The length for V2, the heated length, was 0.30 meter. V1 is the total potential difference from one termination assembly to the other.

All six of these data sets display the behavior of the conductors during the evolution of a nonrecoverable normal zone, initiated by the application of a heat pulse along a 0.3 m length of the outside surface of the conduit. The time constant of the capacitive discharge pulse, RC $\approx$ 0.005 s.

The most obvious characteristic difference between the behavior of the two different conductors can be seen by comparing the plots for shots 193 and 209, taken with the same values of transport current (I = 2.5 kA, $I_{op}/I_c \approx 0.4$), and background field (7T):

- In shot 193, the progressive onset of current sharing along the length of the sample is clearly evident in this unsleeved CICC, reaching the last turn of the coil more than two seconds following the heater pulse. This corresponds to an average normal zone propagation velocity of about 3.7 m/s. Current sharing grows rapidly and uniformly, as evidenced by the initial slopes, steep and featureless, of the curves V3—V5. The curve V1, the voltage across the entire sample length, is also smooth and featureless, showing a 'knee' at the same value of time that corresponds to the knee in curve V5, the time at which the entire sample is fully normal, i.e., current sharing has ceased.
- In shot 209, by contrast, current sharing is evident throughout this sleeved sample immediately after the heat pulse. As is more clearly evident in the expanded plot in

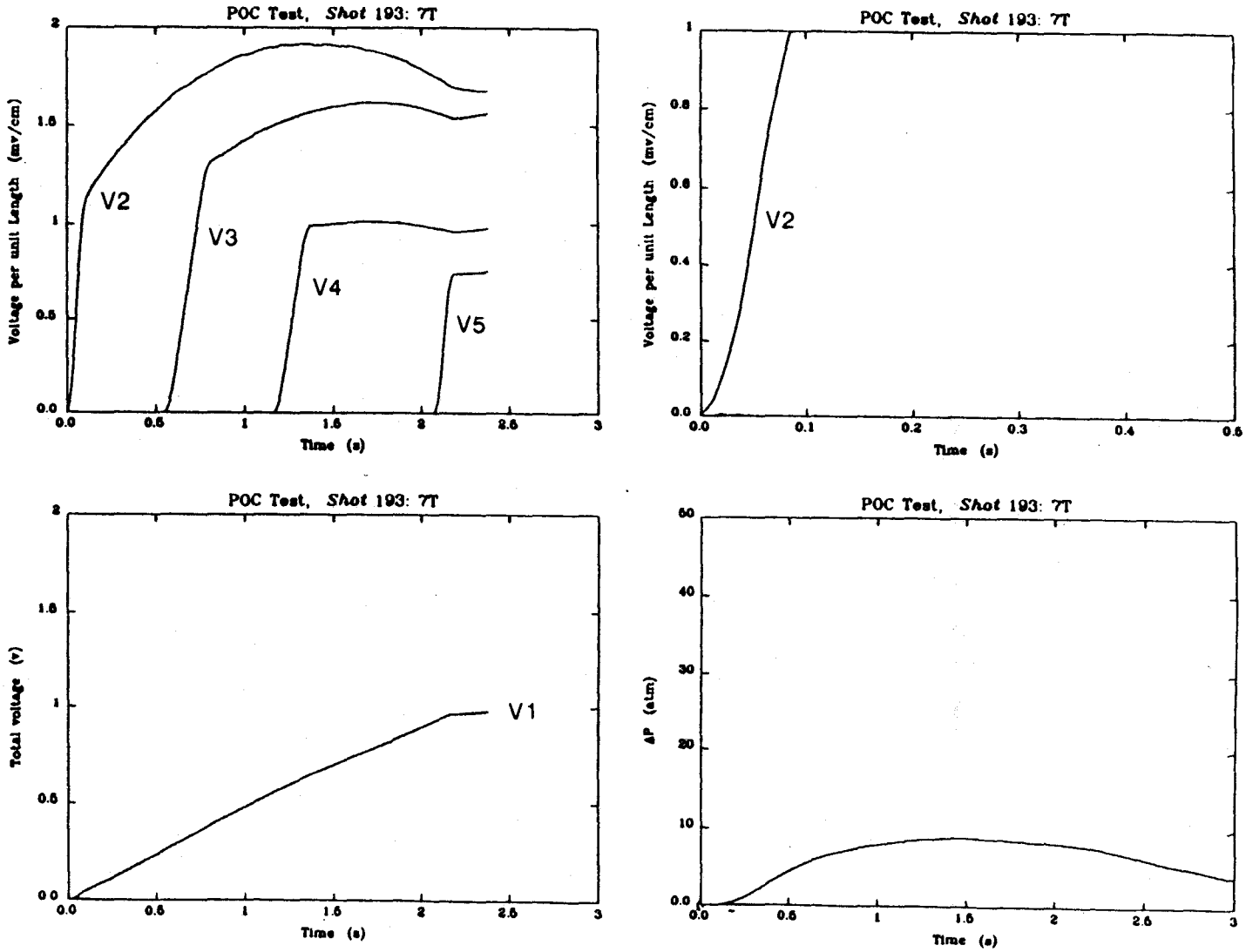

Figure 18
Voltage per Unit Length vs Time for Shot 193

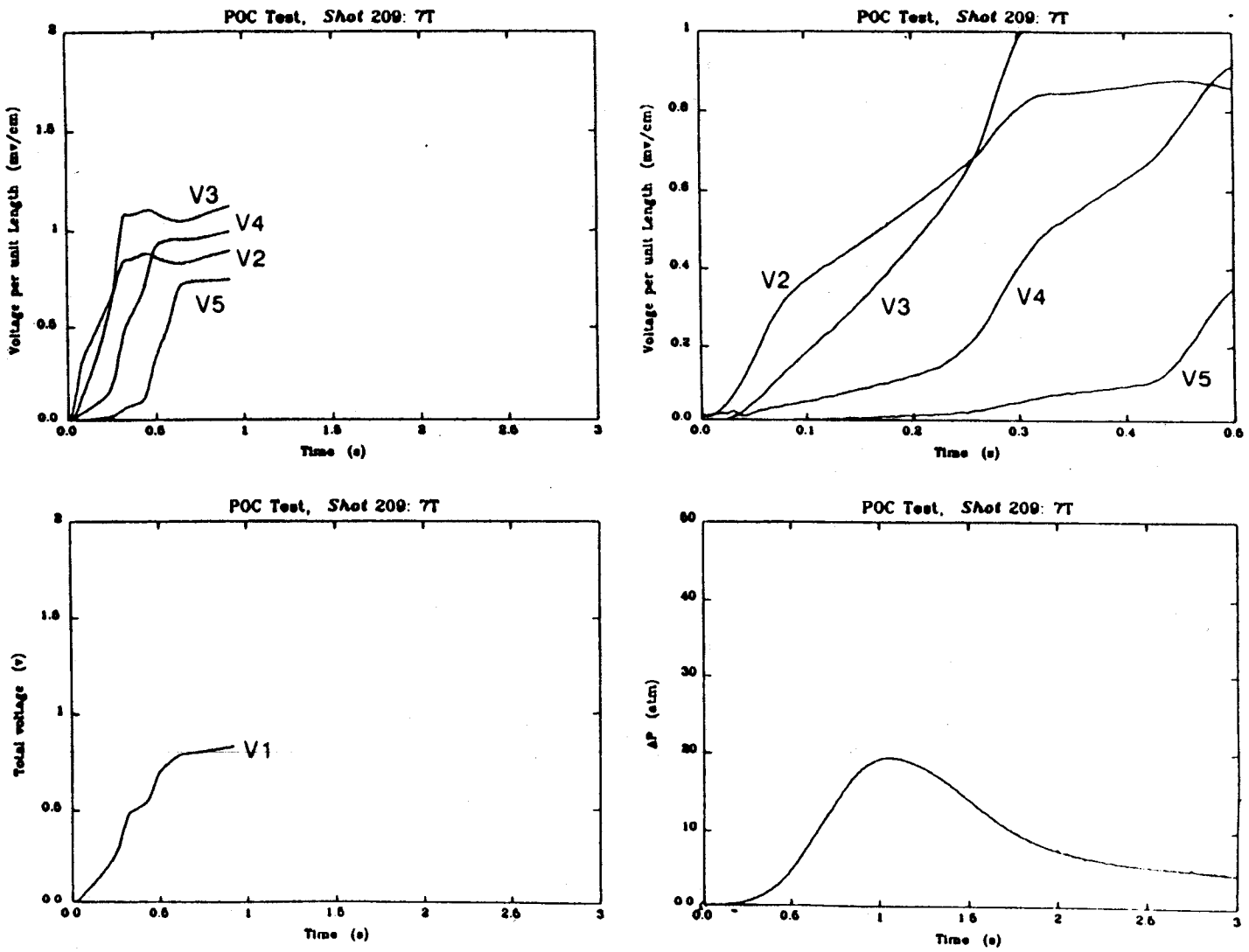

Figure 19
Voltage per Unit Length vs Time for Shot 209

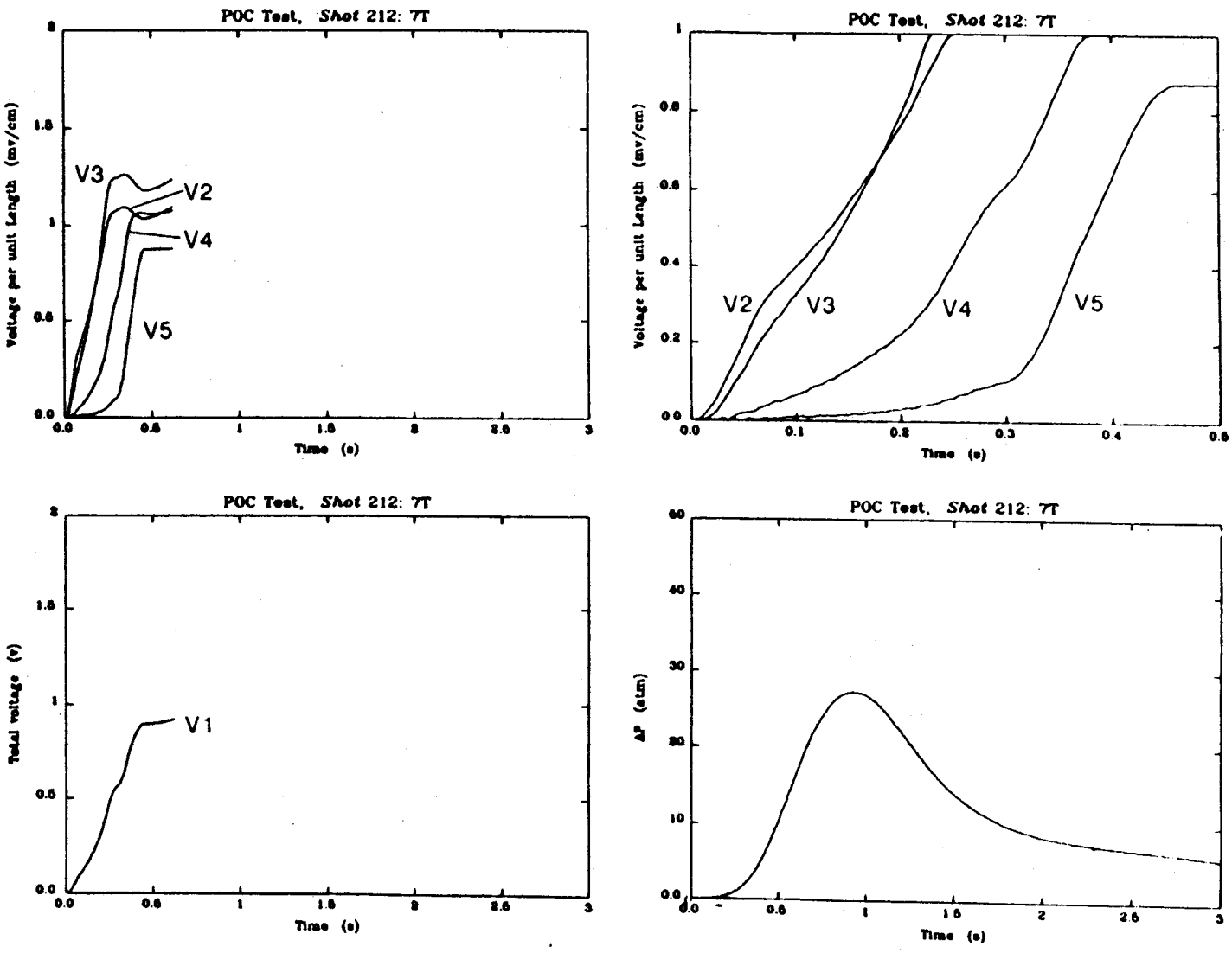

Figure 20
Voltage per Unit Length vs Time for Shot 212

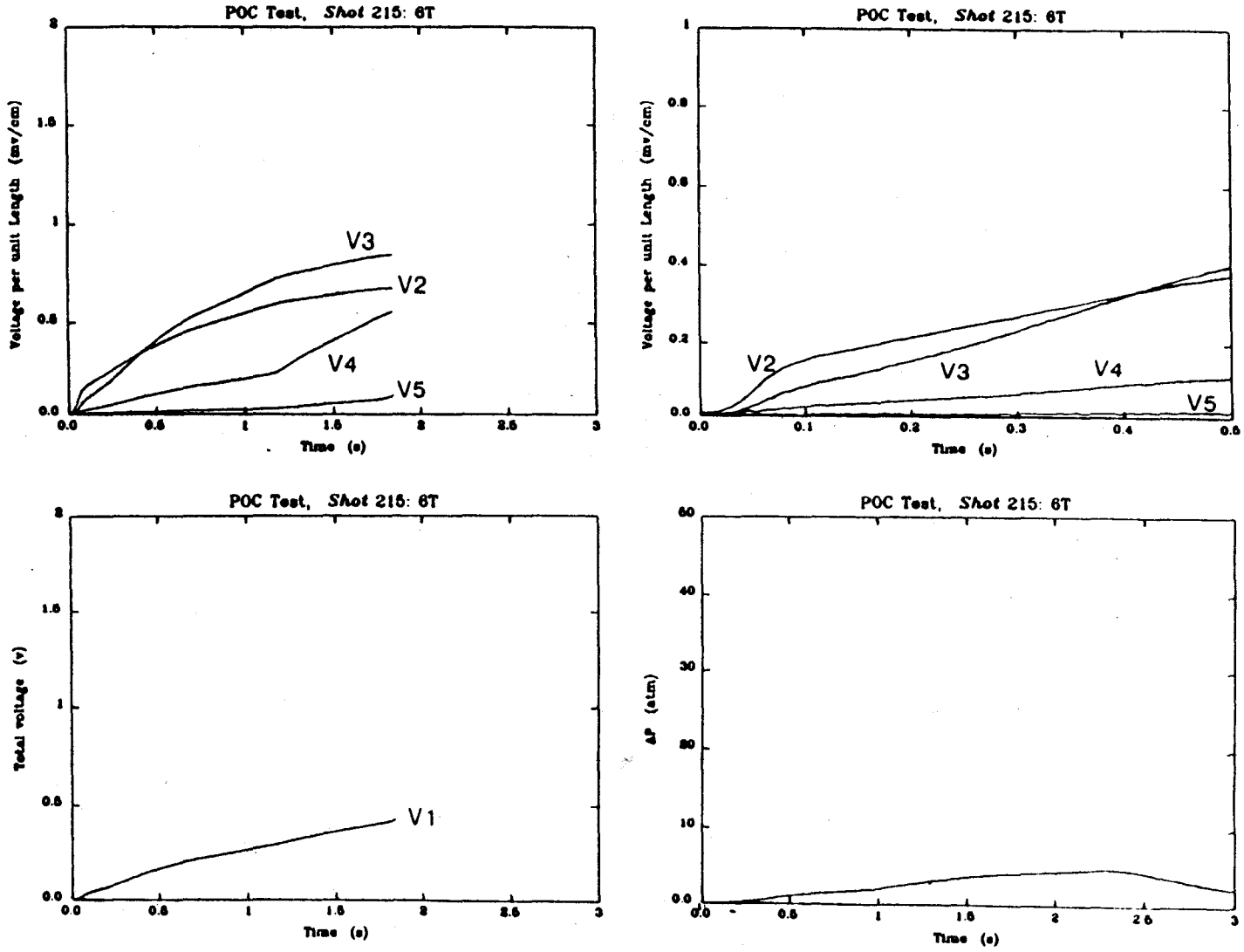

Figure 21
Voltage per Unit Length vs Time for Shot 215

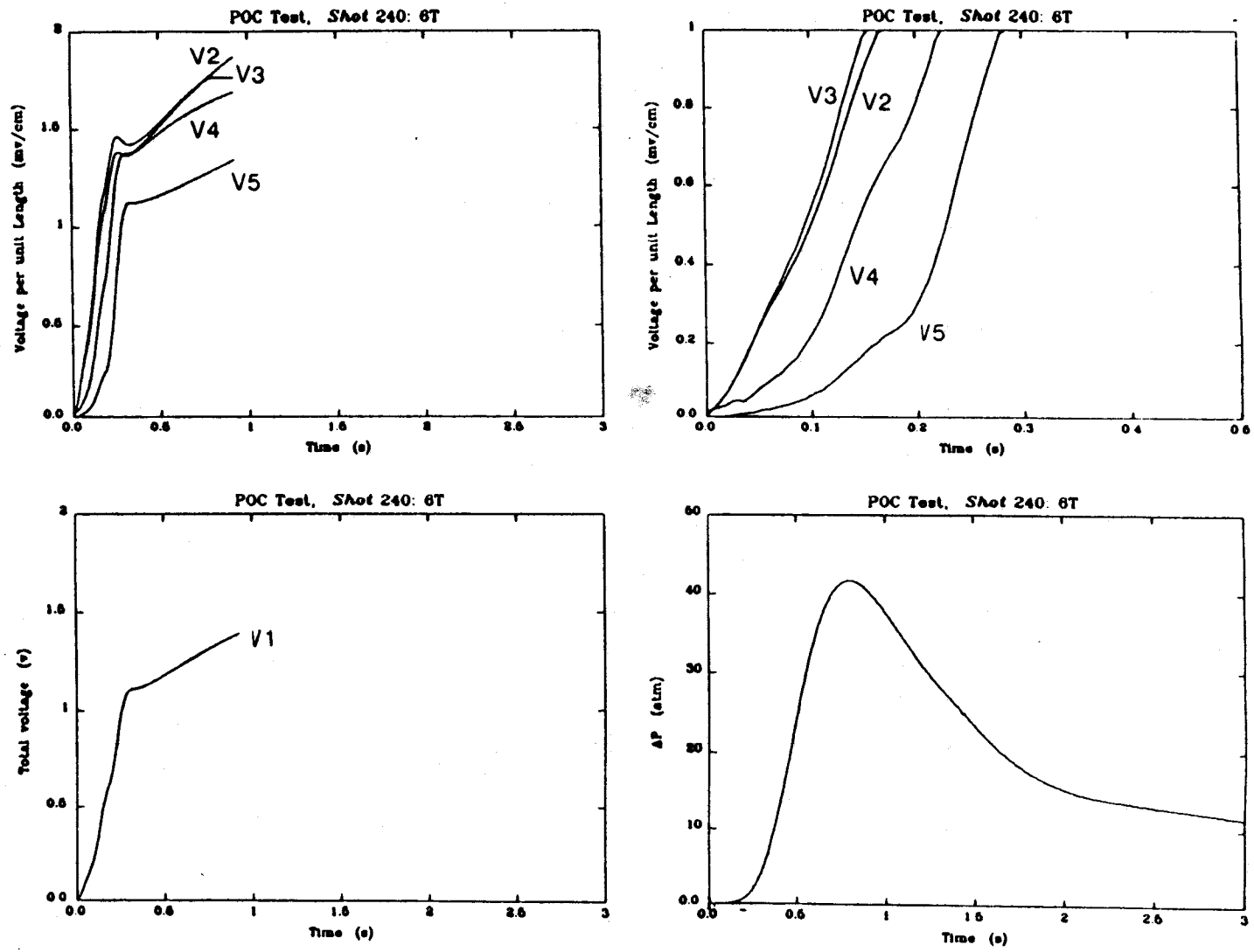

Figure 22
Voltage per Unit Length vs Time for Shot 240

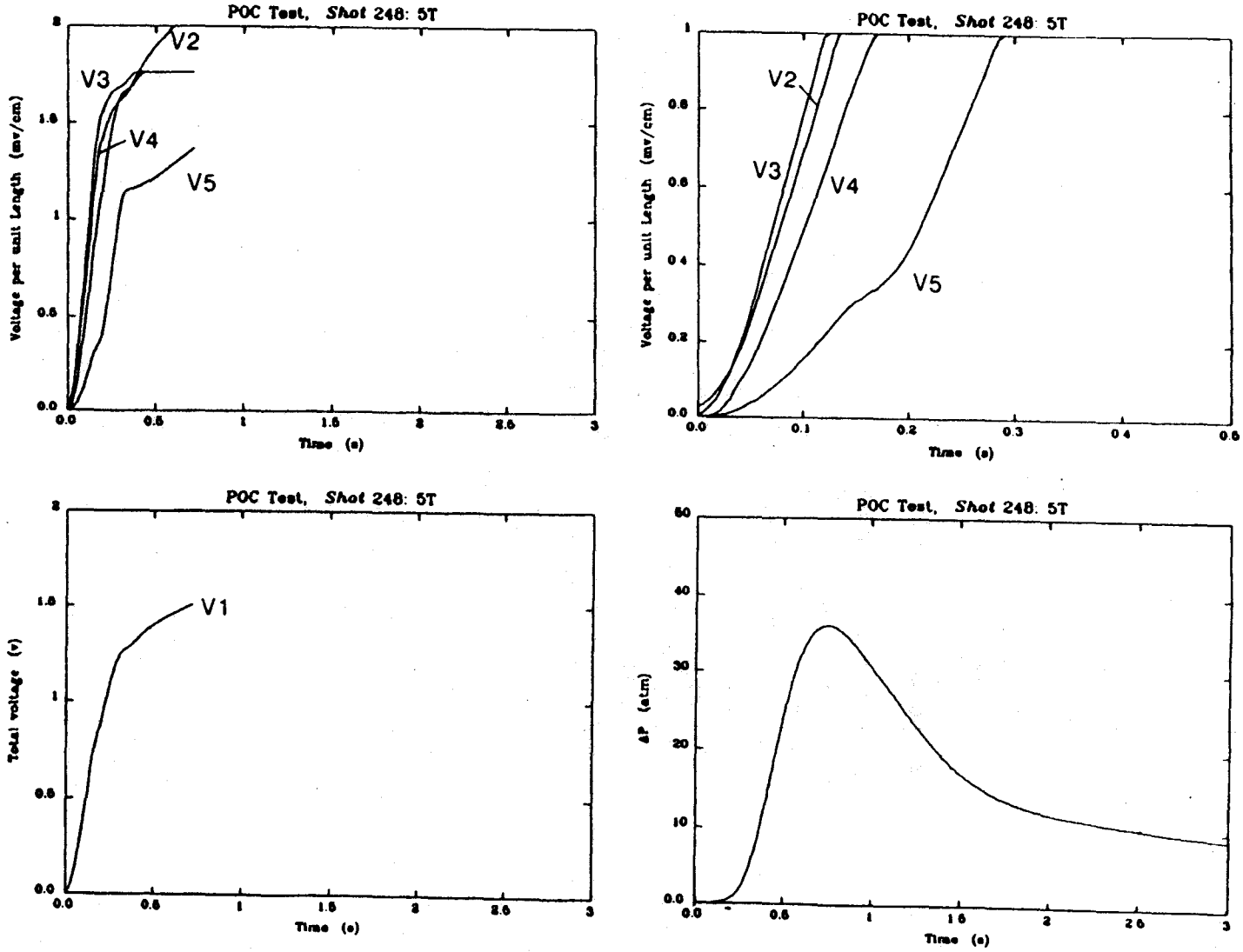

Figure 23
Voltage per Unit Length vs Time for Shot 248

the upper right of the figure, the last turn has begun current sharing after an elapsed time of less than half a second, and has reached T_c at about t = 0.6 s. The concept of propagation velocity would seem inappropriate in ICCSs with sleeved cable, for the transition to the normal state occurs virtually simultaneously over the entire length of the conductor.

These voltage traces are characterized by a more complex shape than those in the previous figure, displaying an early modest slope, followed by a steeper middle section, and finally bending again as the turn becomes fully resistive at the critical temperature. The voltage across the sample terminations, curve V1, also displays this more complex shape; the final slope change in V1 shows that the temperature of the full length of the sample is at least at the critical temperature (6.6 K at 5.5 T) when t $\approx$ 0.6 seconds after the heater pulse.

This comparison suggests that the insulating dacron sleeve has a dramatic effect on the electrical and thermal behavior of this ICCS following a perturbation that exceeds the stability margin. Good electrical contact apparently exists only at the two terminations, as was intended, and as a resistive zone grows in the cable, the resulting potential difference between the two ends of the sample drives current through the full length of the conduit. By this mechanism, the entire length of cable is driven into the current-sharing mode. In an actual inductively-wound magnet, the stored energy would thereby be dissipated over the whole of the volume of conductor, limiting the maximum temperature excursion to a safe value. The current-sharing mode appears to last longer, however, at distances more remote from the site of the initial disturbance, possibly because the dacron sleeve was not woven densely enough to preclude occasional 'soft' electrical shorts.

Next, we compare two shots with the sleeved ICCS taken at the same background field, but with different transport currents, shots 209 and 212:

- The voltage traces all show the same characteristic shapes in both cases, but for the higher current example, shot 212, the slopes of the curves are greater, and hence, as would be expected, the curve V5 indicates that the conductor was fully resistive at an earlier elapsed time than was the case in shot 209.

Comparing shots 215 and 240, both taken at 6 T, but with different values of transport current:

- Once again, the most striking differences between these two sets of data are the slopes of the voltage traces. In both cases, the entire length of the sample begins current-sharing at very nearly the same time, but in the higher current case, the curves are more closely clustered, indicating that at higher values of I_{op}/I_c, the more nearly uniform the temperature would be over the entire volume of the coil.

  This clustering of the voltage traces is even more evident in the plots for shot 248.

3.4.3 Quantitative Analysis of POC Test Data

As an aid to learning as much as possible from the data, two additional sets of plots

were drawn for each quench event, power dissipation per unit length vs. time, Figures 24 — 29, and cumulative energy deposition per unit length vs. time, Figures 30 — 35. This section will describe in more detail some of the quantitative aspects of two of them, shots 193 and 209. These curves are shown in Figures 18, 19, 24, 25, 30 and 31. The power vs. time curve was calculated by multiplying the transport current and potential drop point by point. The cumulative energy deposition was calculated by appropriate numerical integration and summing of the power curve data. All values are presented in terms of a unit length of conductor.

In the case of shot 193, the cable and the conduit were in intimate electrical and thermal contact along the entire length of the sample. Along any length in which the temperature of the strands, $T > T_{cs}$, that portion of the current that could not flow within the superconducting filaments transferred to the copper portion of the strands and to the adjacent section of copper conduit, giving rise to the measured potential drop. Note that no voltage is measured unless and until $T > T_{cs}$ along at least some portion of the length of conductor between a given pair of voltage taps.

Table 3.4-3 summarizes the relevant physical parameters of the unsleeved, or conventional ICCS:

Table 3.4-3
Conductor Data: Shot 193

$A_{strands}$, cm^3/cm	0.123
void fraction	0.38
A_{helium}, cm^3/cm	0.075
m_{helium}, g/cm	9.4×10^{-3}
I_{op}/I_c	≈ 0.4
T_{cs}, K	5.25
T_c, K	6.1
H_{He}(5.25-6.1), J/g	5
H_{He}(5.25-6.1), J/cm	0.047

The listed values of enthalpy per unit length are estimates only, inasmuch as the pressure and temperature of the helium during the course of the event are not precisely known. The enthalpy in the range only from T_{cs} to T_c is relevant here, because no voltage is measured along a given length until the temperature of the cable in that section reaches T_{cs}.

The abrupt change in slope of the traces occurs when the temperature of the strands reaches T_c. For trace V4, for example, this happens at $t \approx 1.3$ s. From the plot of cumulative energy deposition, one can see that by that time, ≈ 0.13 J/cm has been dissipated at that location in the coil. This amount is a factor of three more that the rough estimate of 0.047 J/cm required to raise the helium temperature from T_{cs}, when the voltage first appears across this section, to T_c. The discrepancy could be the result of some heat conduction through the insulating cocoon-like shell that was intended to isolate the coil from the helium bath.

The values for the corresponding shot with the sleeved conductor are listed in Table

3.3-4:

Table 3.3-4
Conductor Data: Shot 209

$A_{strands}$, cm^3/cm	0.123
void fraction	0.33
A_{helium}, cm^3/cm	0.066
m_{helium}, g/cm	8.2×10^{-3}
I_{op}/I_c	≈ 0.4
T_{cs}, K	5.25
T_c, K	6.1
H_{He}(4.2-5.25), J/g	28.1
H_{He}(4.2-5.25), J/cm	0.23

For this shot, the enthalpy of interest is that required to raise the temperature from 4.2 K to 5.25 K, that is, the energy required to drive the strands into a nonrecoverable current-sharing mode. For, as explained in an earlier section, once a resistive region develops anywhere in the conductor, the resulting terminal potential difference drives some of the current through the entire length of conduit, and a voltage is detectable at every one of the voltage taps simultaneously, whether or not the cable is resistive at that particular location.

In this case, the resistivity of the conduit material must be known in order to calculate the power that it dissipates in any given length. For this purpose, a spare piece of the conduit that had the same history of cold work as the sample conduit was instrumented for resistivity measurements. Data was taken at room temperature and at 77 K. These results, combined with published data on this alloy of copper, yielded a best estimate of 0.5 $\mu\Omega$-cm for the resistivity of the conduit at 4.2 K. The magnetoresistance is believed to be small compared to other uncertainties in this analysis, as is the temperature dependance of the resistance over the range of interest here, 4.2 K — 10 K. The conductor length for V3, V4, and V5 each correspond to one turn, or about 0.56 meter. The length for V2 is the heated length, 0.30 meter. V1 is measured across the entire sample length from one termination assembly to the other, a length of about 8.2 m.

The resistance for each length spanned by voltage taps, then, was calculated, and made constant for purposes of calculating the power dissipation during the initial quench transient; the power was obtained by taking the quotient V^2/R for each section, data point by data point. It is important to emphasize the difference between this case and the previous one: the only joule heating that occurs at sites remote from the location of the initial perturbation, during the early phases of the quench, is that due to current flowing in the conduit. That current is a comparatively small fraction of the total transport current, a maximum of about 300 A of a total 2.5 kA in shot 209, and flows in the conduit because of the growing potential drop *across the entire sample length* generated by current sharing that began at the site of the initial perturbation.

Inspection of trace V4 in Figure 19 shows two distinct slope changes. The first change

occurs at the onset of current sharing, when $T = T_{cs}$, and the second, when the strands are fully normal, when $T = T_c$. The first slope change occurs at $t \approx 0.22$ s. Referring to the cumulative energy plots in Figure 31, one finds that it is not possible to read a value that early in the transient, except to estimate that $E < 5 \times 10^{-4}$ J/cm. If the energy generated by joule heating in the conduit is absorbed by the interstitial helium, which in turn would raise the temperature of the strands to T_{cs}, then, as listed in Table 3.3-5, 0.23 J/cm would be required. Clearly, current-sharing has begun long before enough energy has been generated in the conduit to raise the temperature of the helium to T_{cs}.

However, it is straightforward to calculate that only about 2.2×10^{-4} J/cm are sufficient to raise the temperature of the conduit and the strands to the current sharing temperature. This suggests that while the dacron sleeve is effective in electrically isolating the strands from the conduit, the intimate physical contact between the sleeved, compacted cable and the ID of the conduit, an inevitable consequence of the method of manufacture, leads to comparatively effective heating of the strands by conduction from the conduit, despite their being immersed in cooler helium. The cable and subcable twist sequence ensures that all strands will be at the OD of the cable at frequent intervals, and hence they all are able to accept heat conducted from the conduit through the dacron barrier.

Stability

One of the intended features of this sleeved cable ICCS was to enhance the stability of the conductor against small friction-induced heat inputs. By introducing a helium-permeable thermal barrier between the conduit—where the frictional heating arises—and the strands, with their very small heat capacity, this design would enable the interstitial helium to play a major role in absorbing externally-applied heat before the vulnerable strands that were immersed in it were driven into current sharing.

Even though the chief thrust of these tests was not a comparison of energy margins of the two configurations, some stability data were taken. (A LHe transfer problem unfortunately curtailed the test of the unsleeved sample before stability data could be taken over the desired range of field and transport current.) The data are shown in Figure 36. Heat pulses that did not produce a nonrecoverable normal zone are indicated by $\diamond$, while those which initiated a quench are drawn as $\times$.

Two aspects of these data should be noted. First, the stability margin of the unsleeved sample is *larger* than that of the sleeved sample, the reverse of prior expectations. Second, the value of energy margin for the higher field cases of the sleeved sample seem strangely constant over the range of I_{op}/I_c covered in the test. These results were unexpected and, as yet, are not fully understood. Further analysis of this stability data will be required.

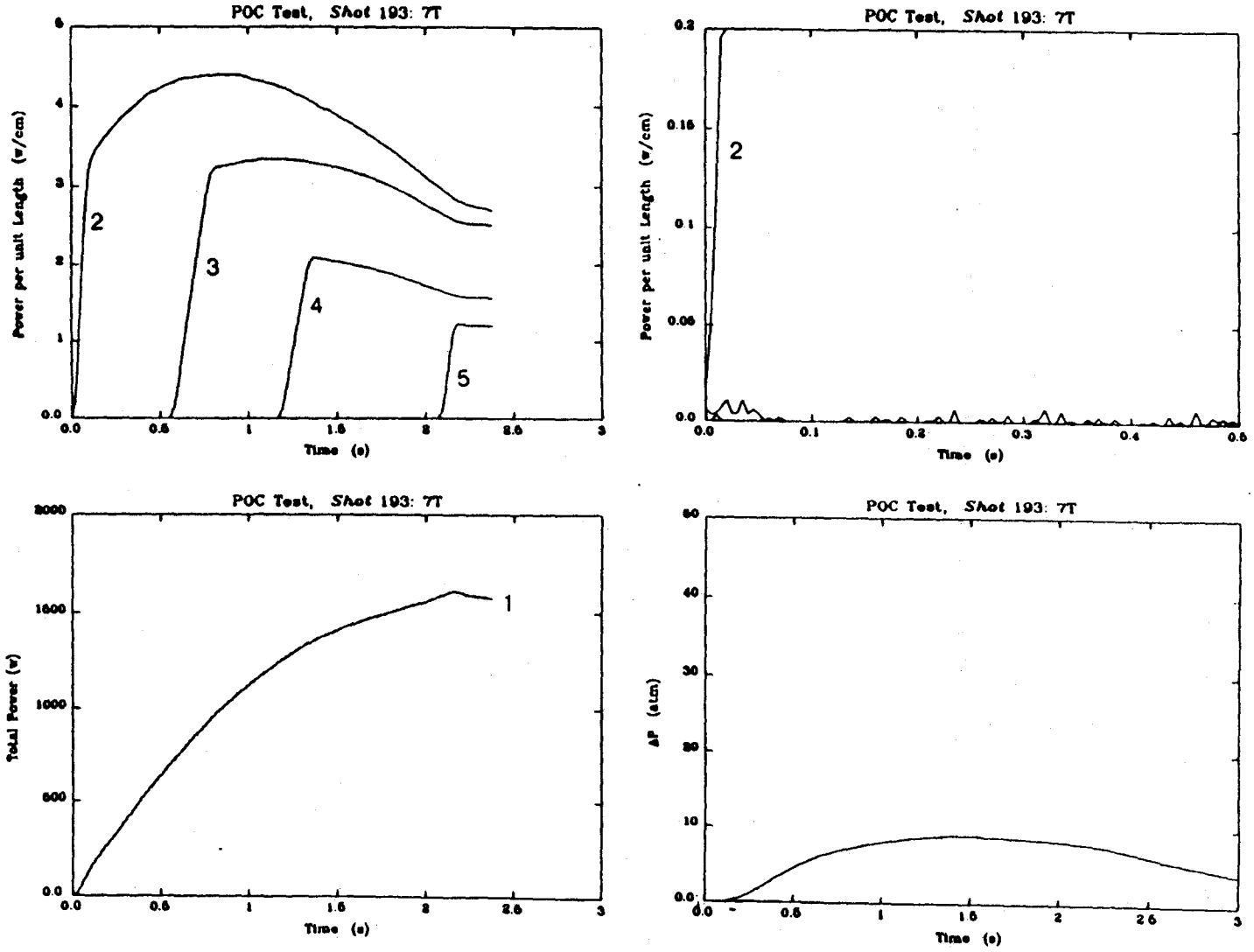

Figure 24
Power per Unit Length vs Time – Shot 193

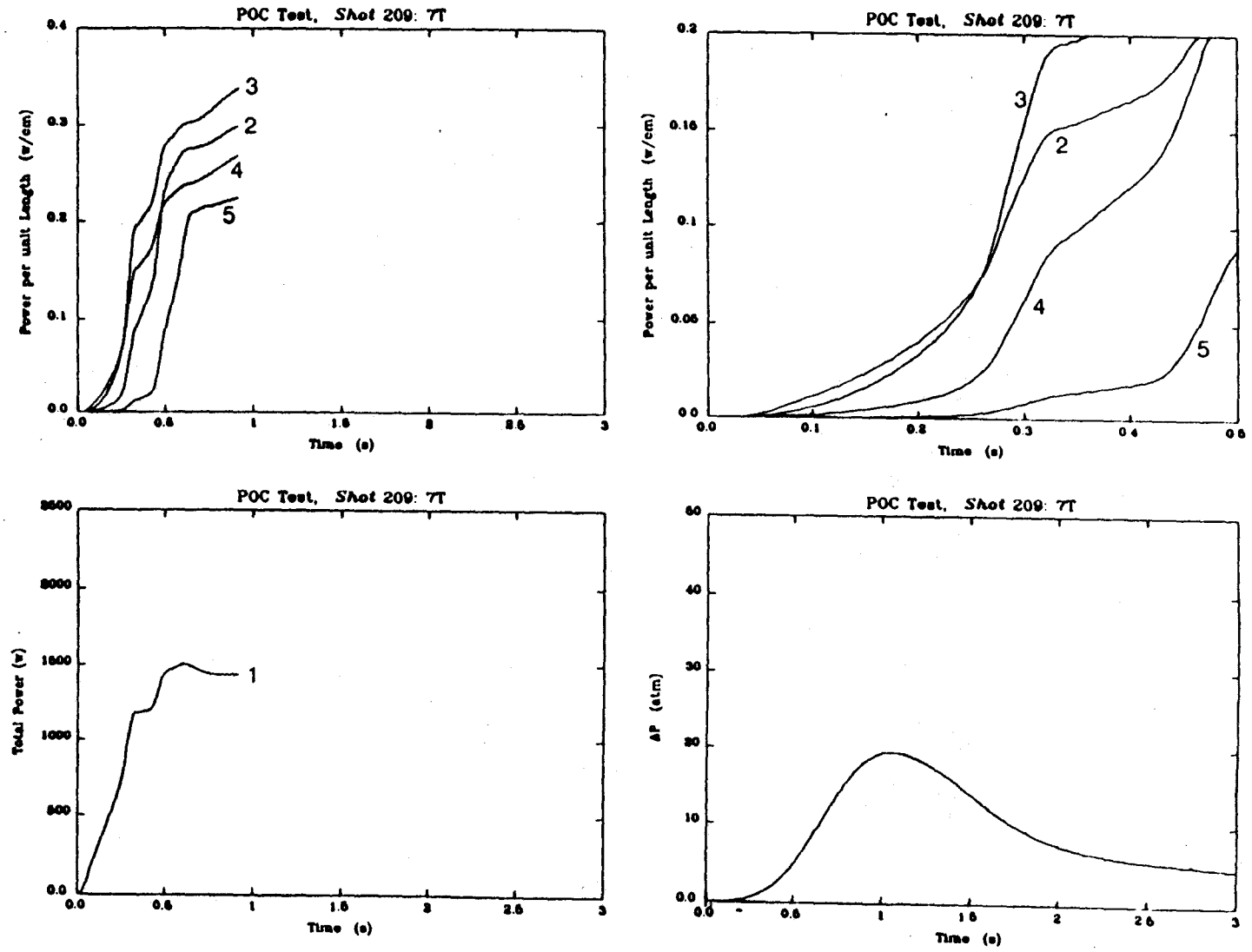

Figure 25
Power per Unit Length vs Time – Shot 209

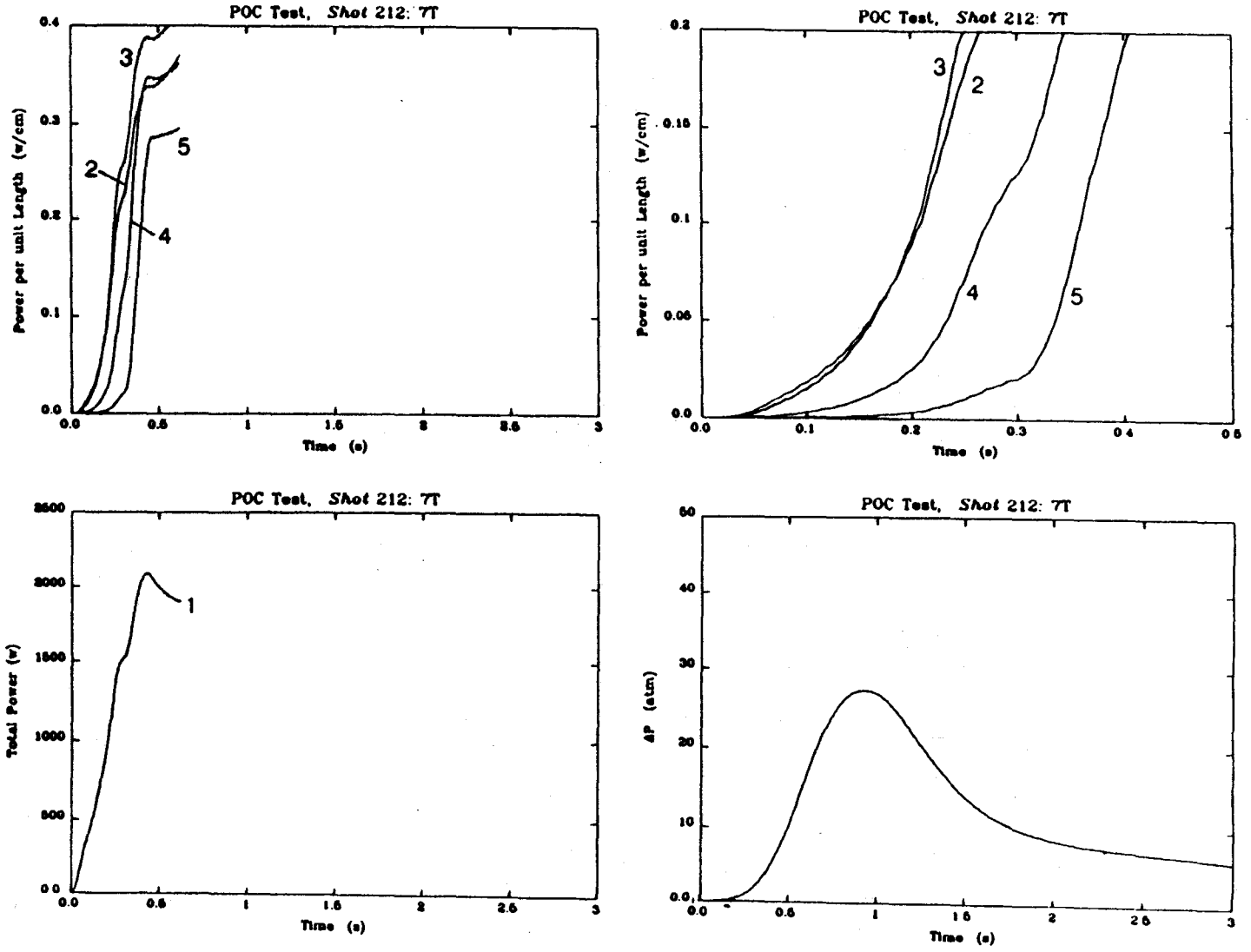

Figure 26
Power per Unit Length vs Time – Shot 212

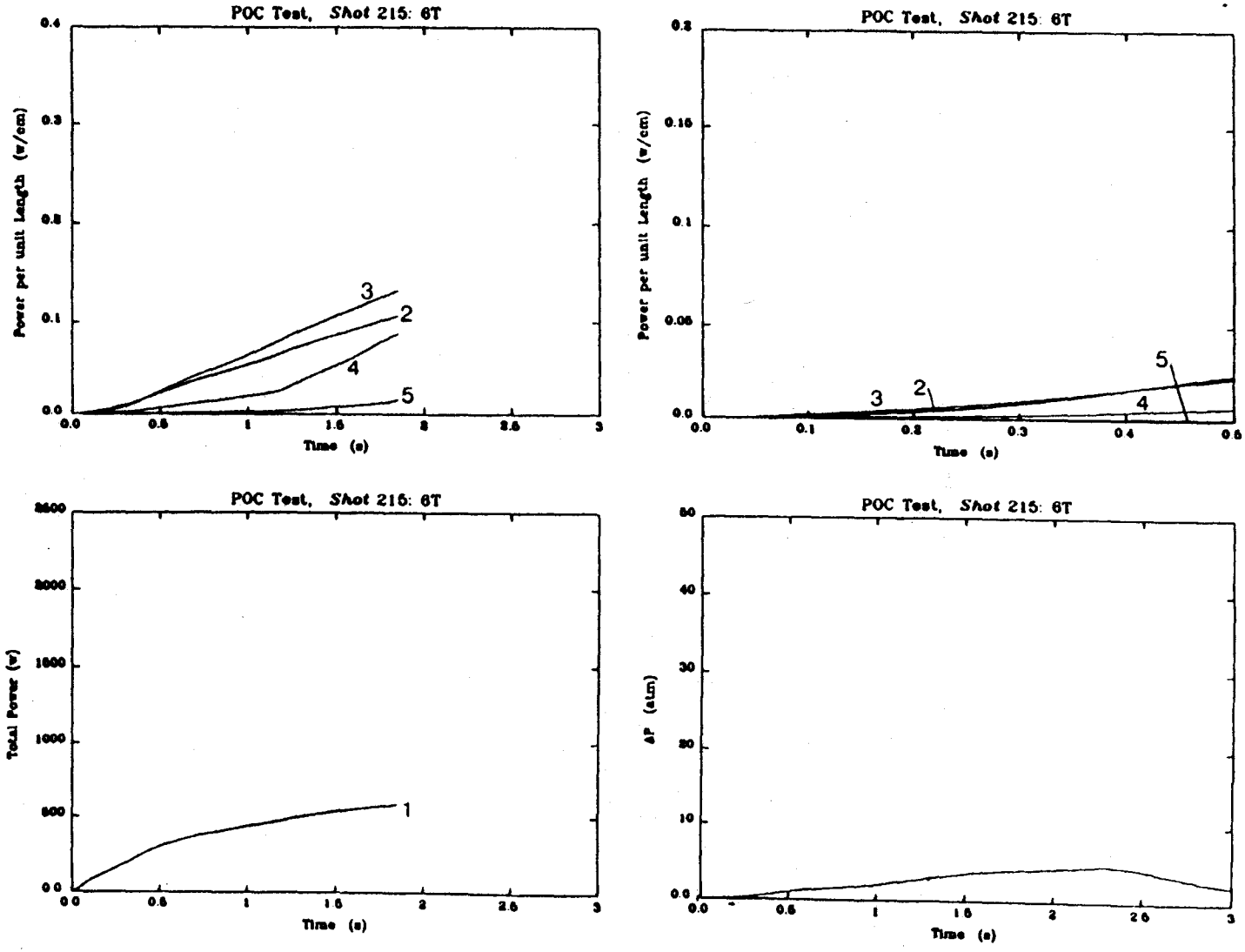

Figure 27
Power per Unit Length vs Time – Shot 215

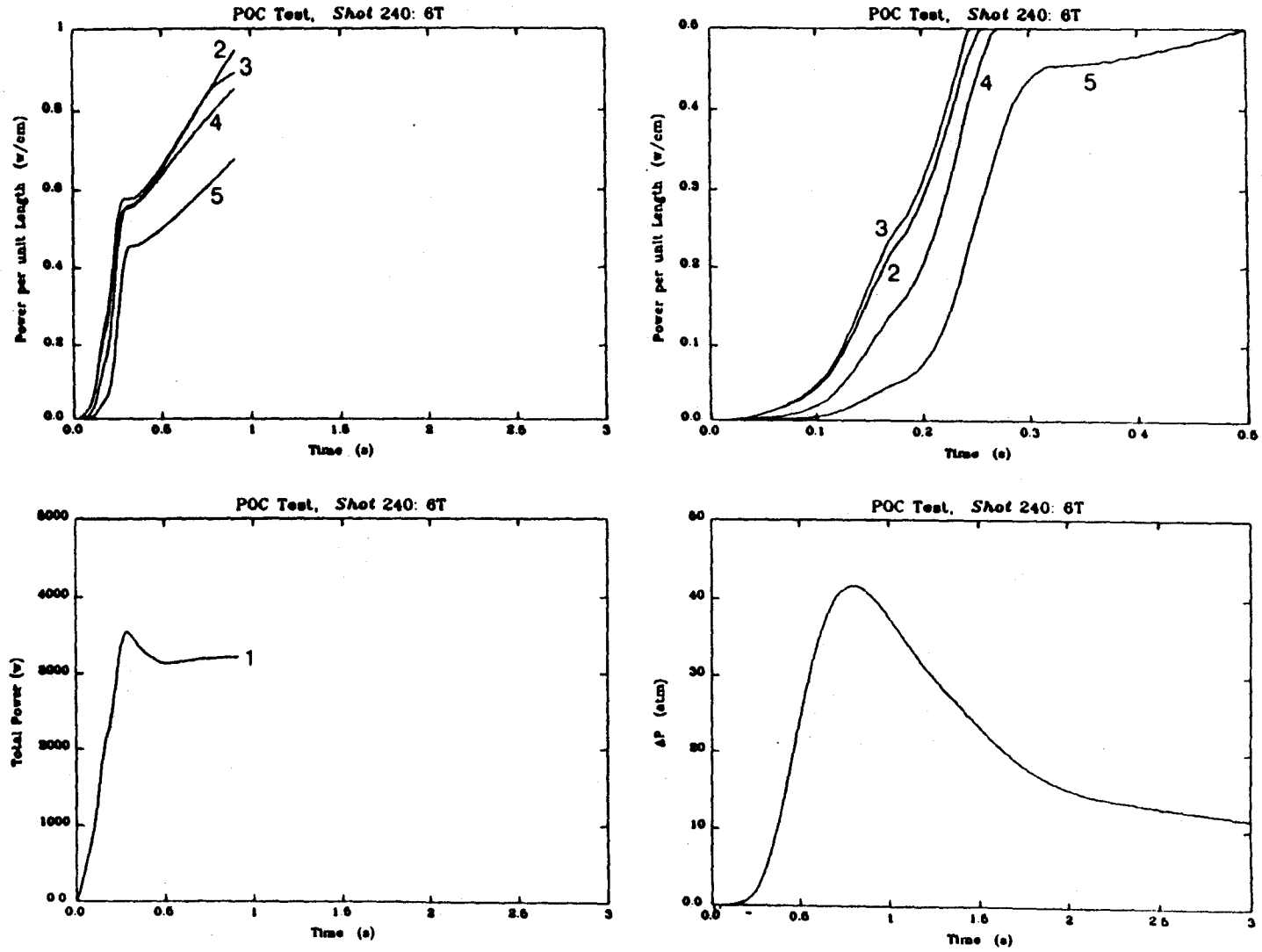

Figure 28
Power per Unit Length vs Time – Shot 240

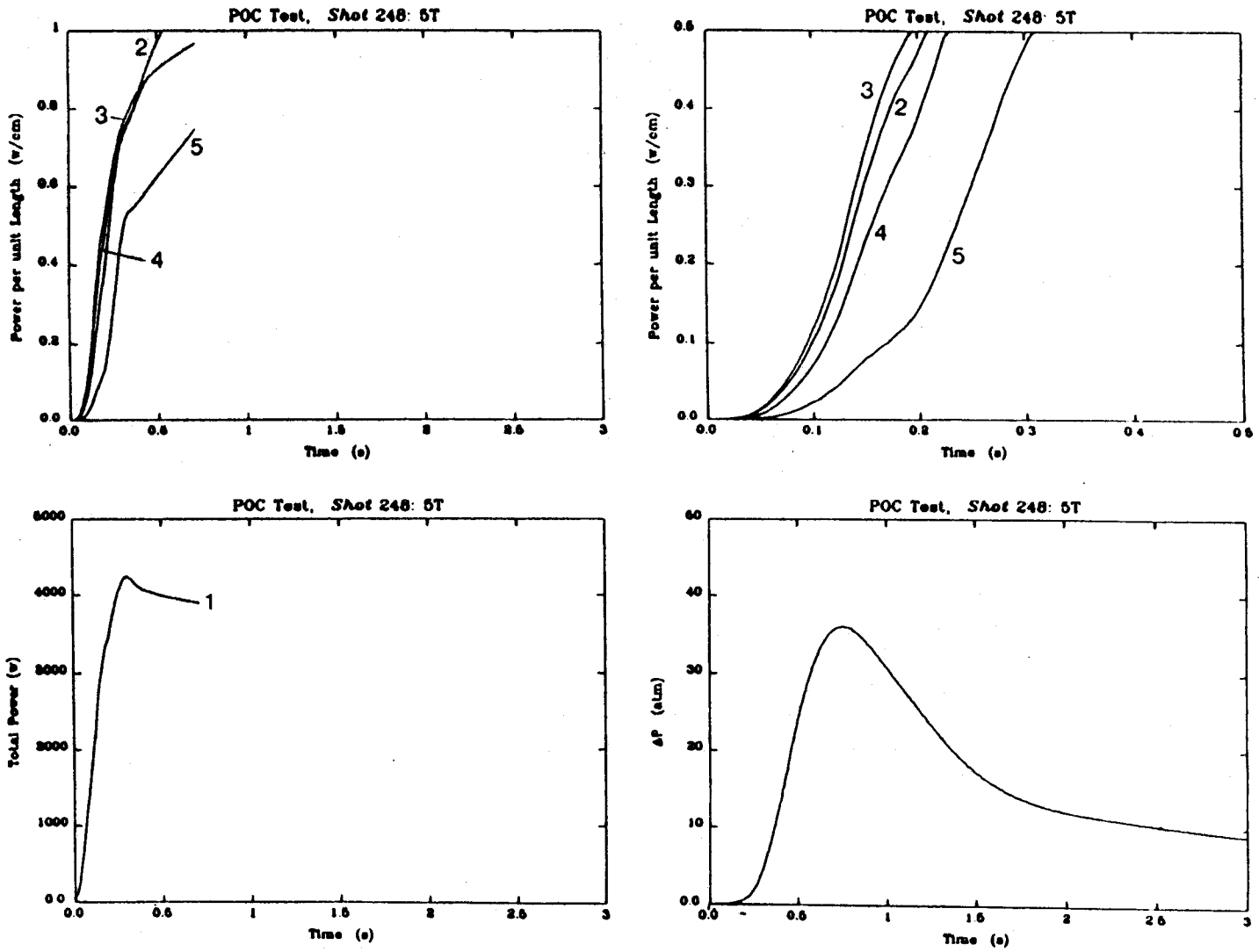

Figure 29
Power per Unit Length vs Time – Shot 248

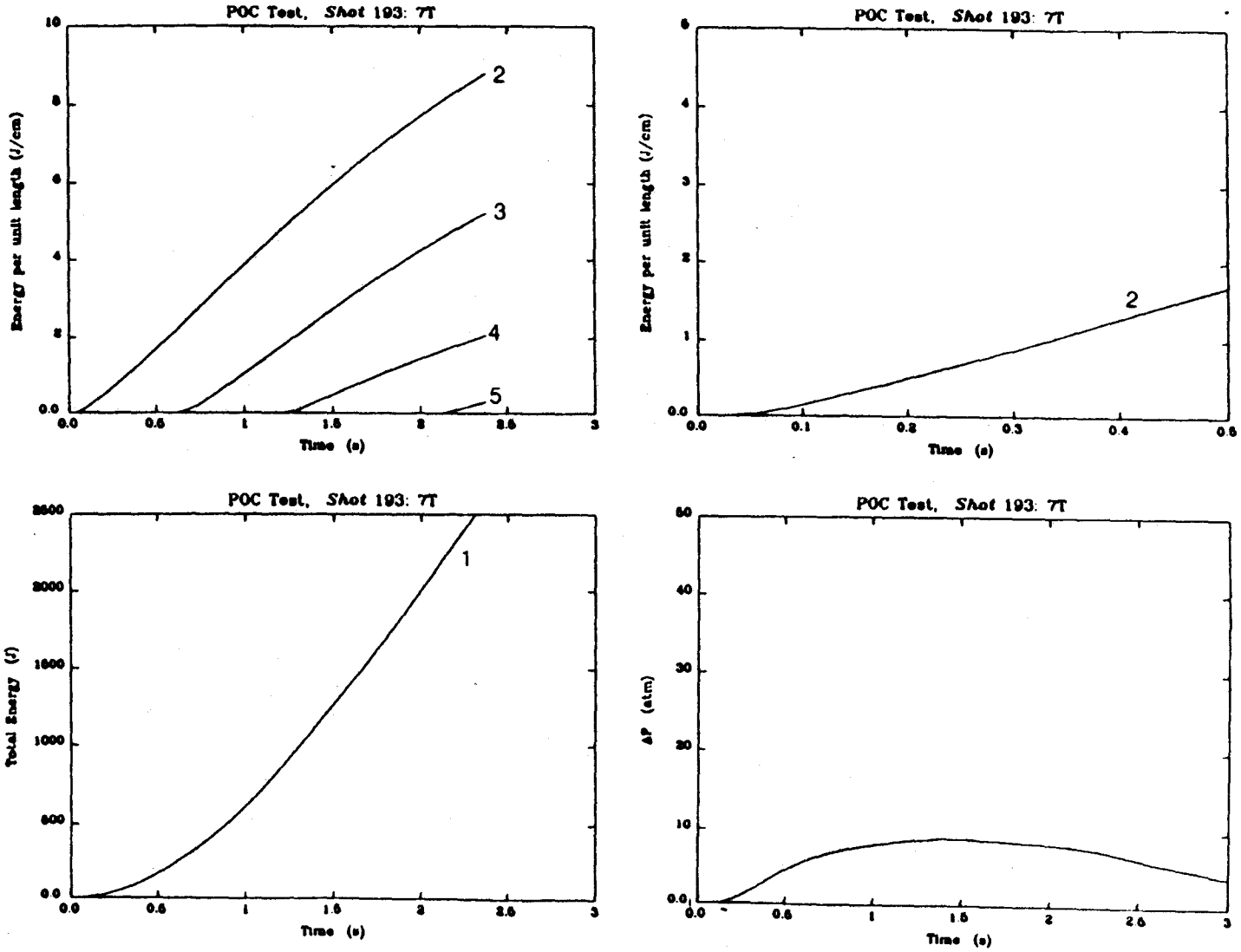

Figure 30
Energy per Unit Length vs Time – Shot 193

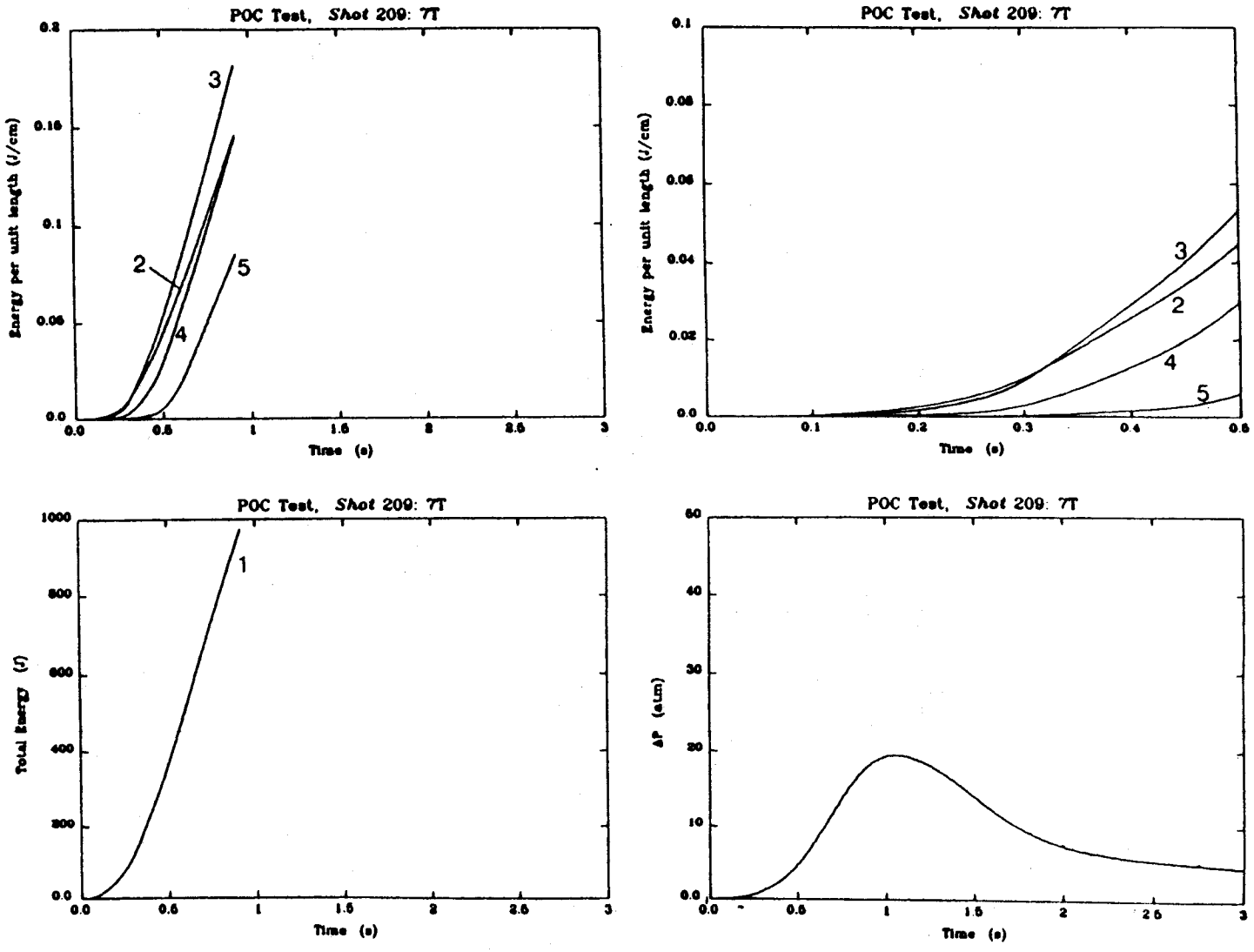

Figure 31
Energy per Unit Length vs Time – Shot 209

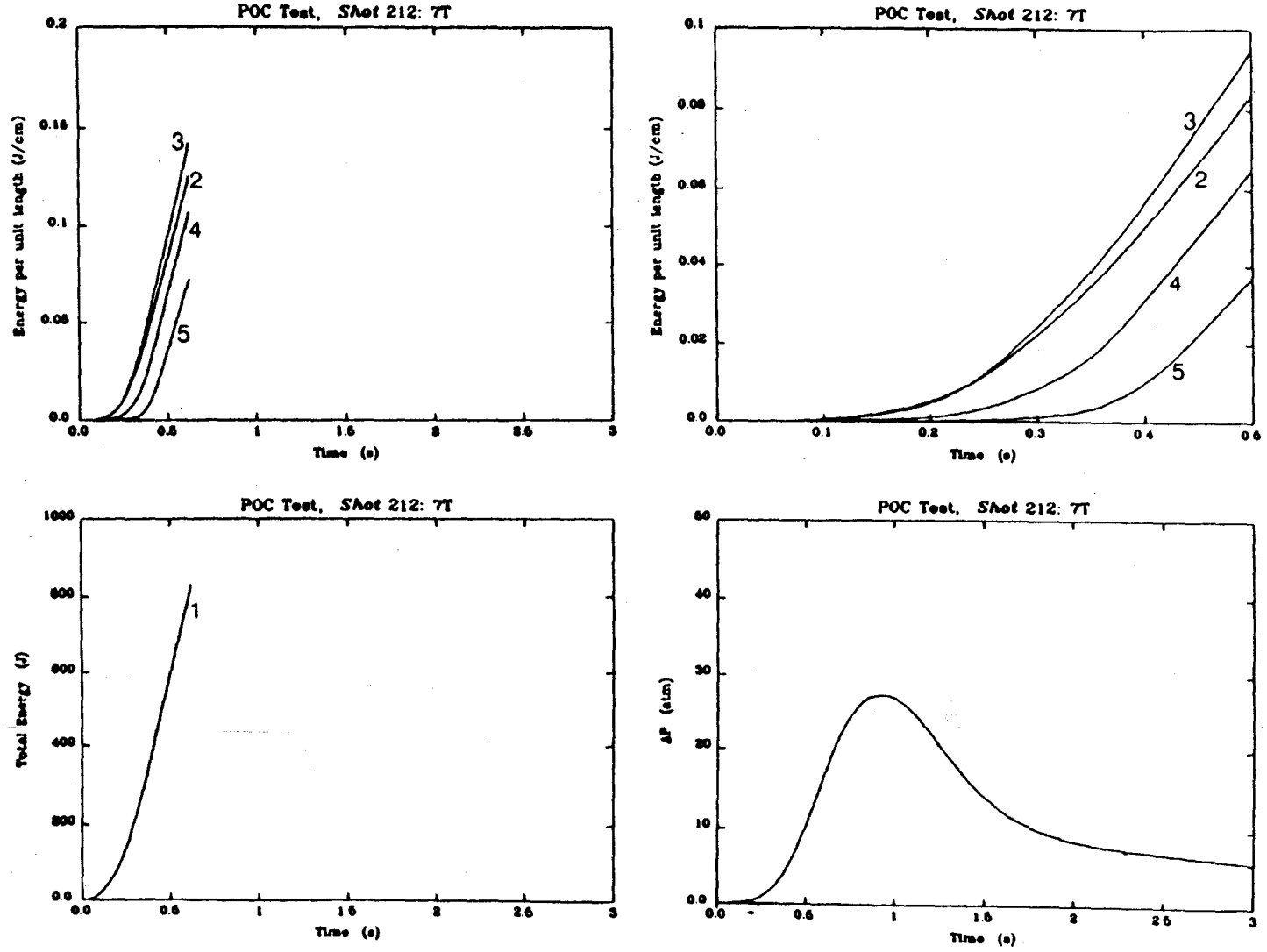

Figure 32
Energy per Unit Length vs Time – Shot 212

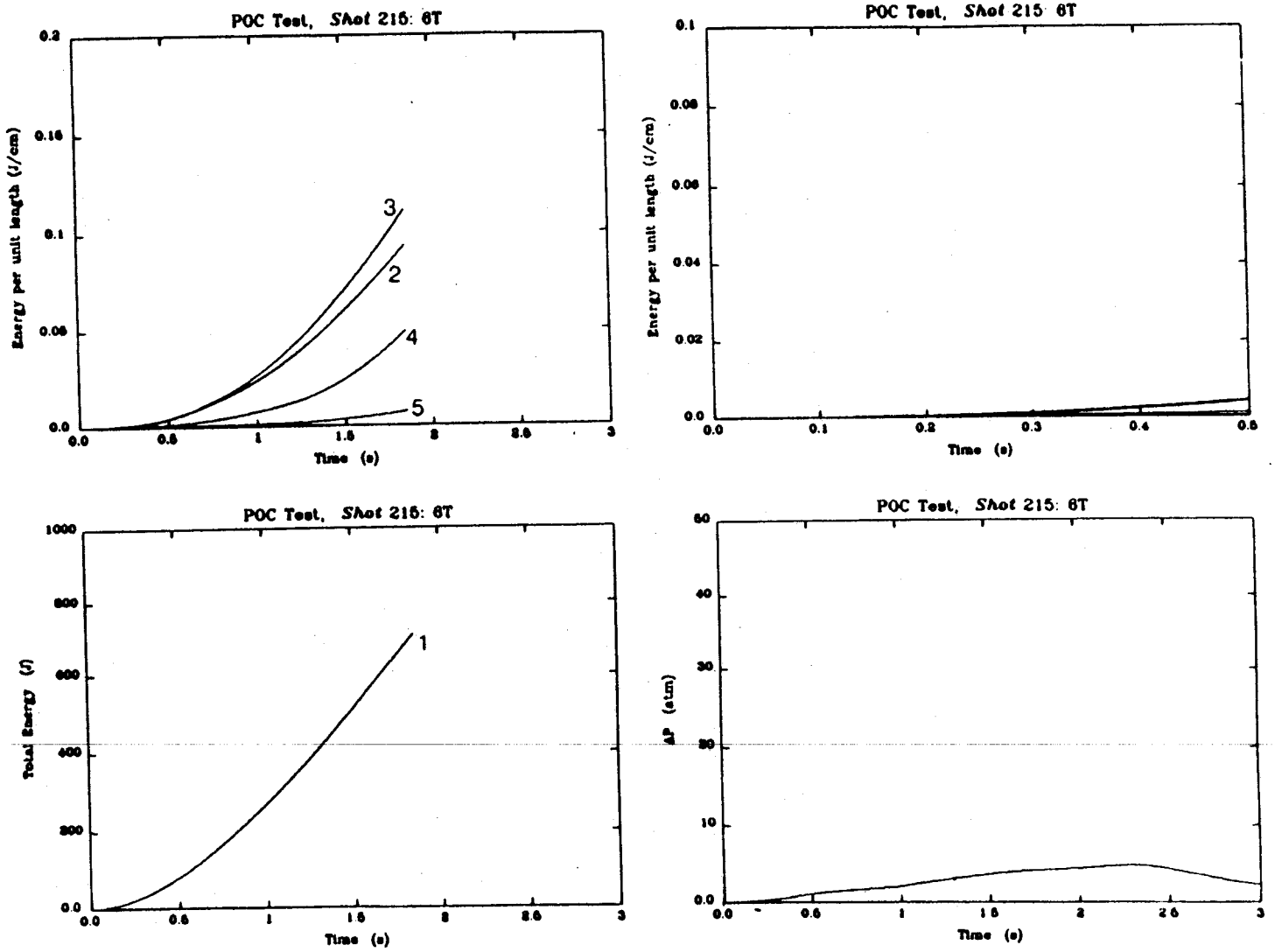

Figure 33
Energy per Unit Length vs Time – Shot 215

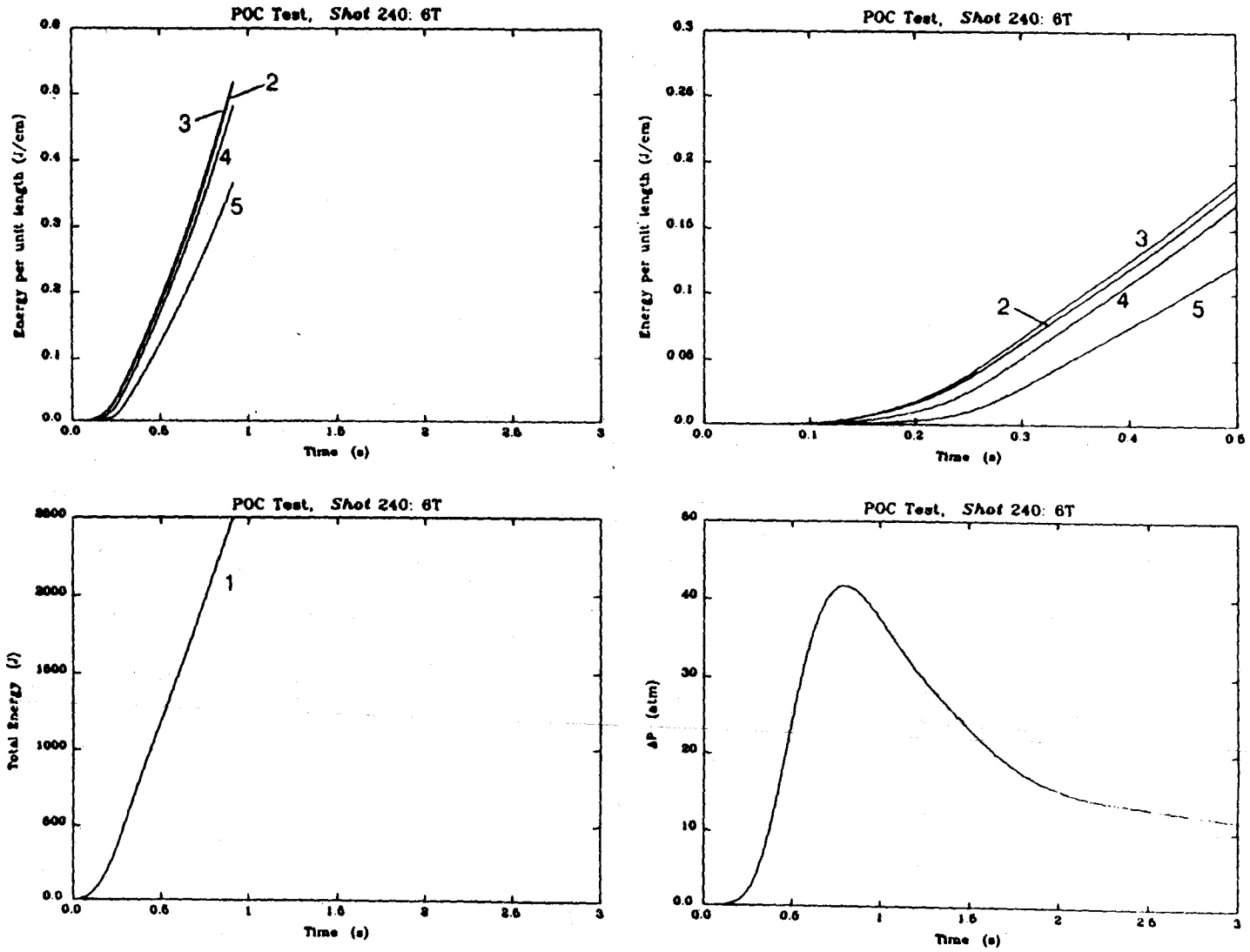

Figure 34
Energy per Unit Length vs Time – Shot 240

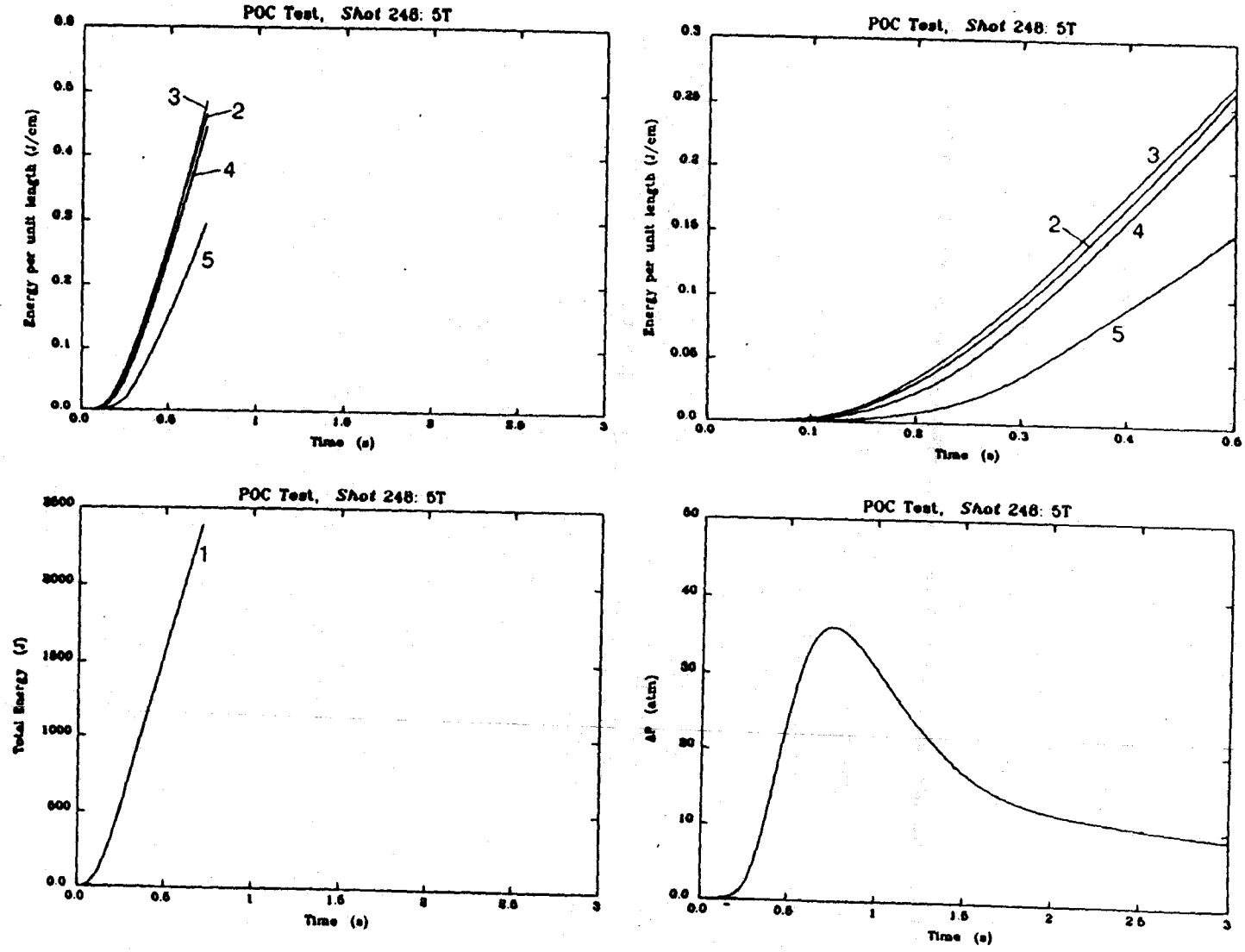

Figure 35
Energy per Unit Length vs Time – Shot 248

4.0 Conclusions and Recommendations

The goal of this program has been to develop a subscale proof-of-concept niobium-titanium (NbTi) internally cooled, cabled superconductor that would be suitable for use in a retrofit-size MHD magnet system. That goal has been achieved through the design and teest of the novel conductor described in this report and in other reports issued during the course of this work. The protection characteristics of this conductor are matched to the protection needs of MHD magnet systems where quench-causing disturbances are generated most commonly by motion between turn or between pancakes.

Comparative testing of two samples of Internally Cooled, Cabled Superconductor has demonstrated the proof of concept for thid novel conductor design. The primary characteristics of this design are:

- Strands with a comparatively small Cu:SC ratio;
- Conduit made with material that has a comparatively low electrical resistivity;
- An electrically insulating, helium-permeable sleeve or barrier interposed between the conduit ID and the superconducting cable.

The meaning of the term 'propagation velocity', as applied to a growing normal zone in a conductor of this configuration, is nebulous at best, for the transition to the normal state does not progress from one location to the next along the length, so much as it progresses in time over the whole length at once.

The behavior of this conductor under fault conditions in an inductive device would be characterized by a quench that dissipates the stored energy over the entire volume of the device in a comparatively short span of time. Such a global quench could well be further enhanced by phenomena that did not occur in these modest-scale tests, among them being inductive quench-back, which would increase the amount of current in the conduit, and thermohydraulic quench-back.

The next requirement in the on-going development of this conductor would be to devise a mathematical model, and computer codes for numerical simulation of the electrical, thermal, and hydraulic behavior of a ICCS of this design. Materials optimization, manufacturing development, and magnet fabrication techniques also require careful attention before large-scale devices can be built and tested.

A well-designed computer simulation is essential to the understanding of the role played by the barrier layer, both in stability phenomena and in the protection of a device during a quench. The dacron barrier in the test conductor described herein was almost surely not optimum; it appears to have not enhanced the stability margin; however, it dramatically improved the protection characteristics of the conductor. Barriers of different materials, thicknesses, and physical configurations could, in principle, be explored by utilizing a good computer code, and thereby, a more suitable balance between stability enhancement and protection could be achieved. The simulation code would also be essential in the determination of the optimum length and conduit cross section of a conductor for a given application that would perform in the desired manner during a quench.

Copper was chosen as the low resistivity material for the conduit for these test samples because of the ease of fabrication and availability. For use in large-scale devices such as MHD topping cycle facilities, conductors of this configuration would most likely use a high-strength aluminum alloy. The selection of the most suitable alloy, and the development of a cost-effective manufacturing and fabrication technology for its utilization will be an important facet of the overall conductor development program.

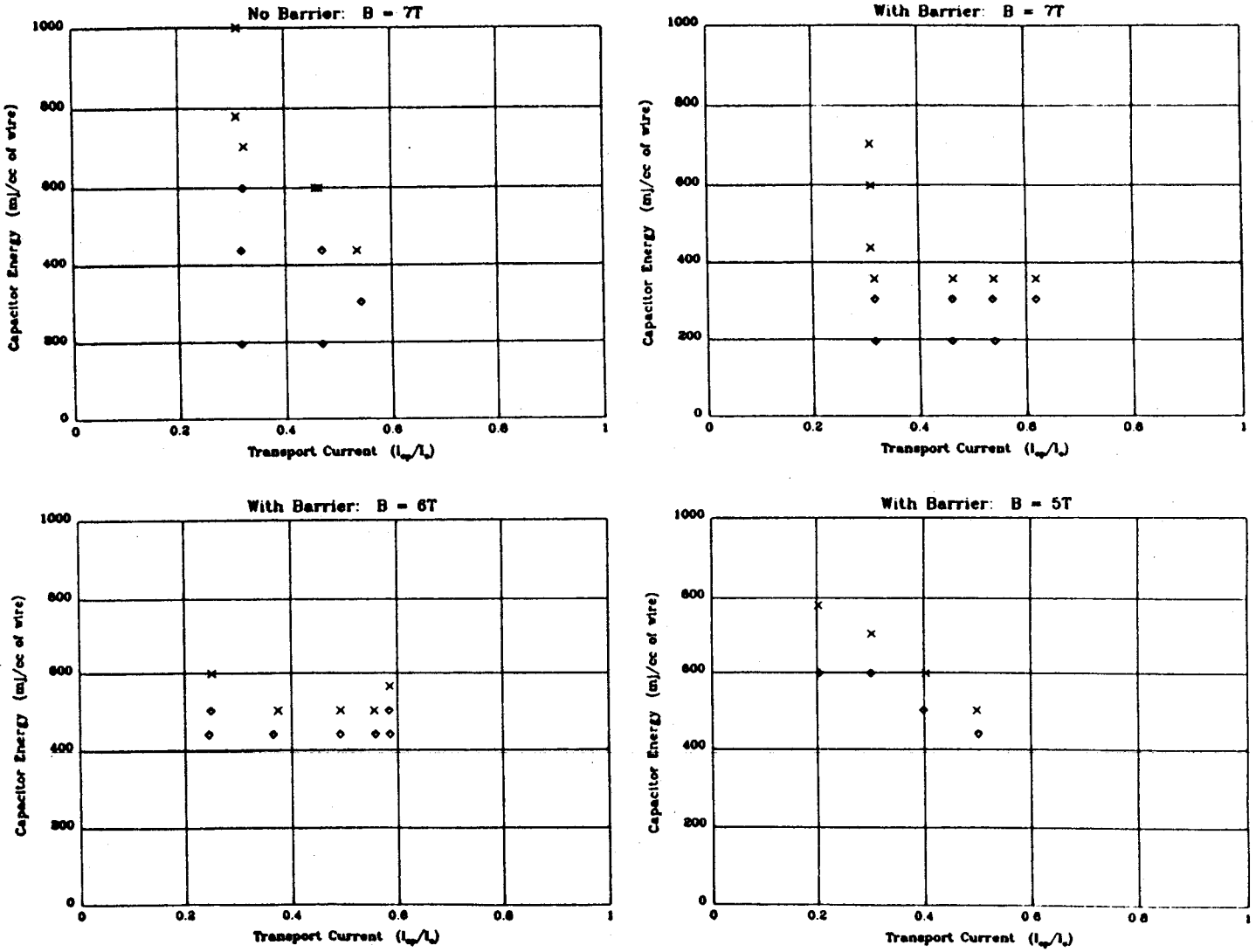

Figure 36
Stability Data for Unsleeved and Sleeved Conductor

Detailed Descriptions of Selected Figures

Figure 13. Longitudinal section of dewar, showing the sample coil in position relative to the gas-cooled lead assembly. The 10" tail of the dewar fit the bore of a 10 MW Bitter magnet that generated background magnetic field of up to 7 T.

Figure 14. Electrical schematic of test coil, showing the location of heater, the pressure transducer, and connection points for five voltage tap pairs. The coil was wound as a single-layer noninductive double helix on a grooved G-10 mandrel.

Figure 15. Schematic representation of data acquisition system. Identification of the nine data channels is given in Table ___. Data that was stored in the VAXstation during the experiment was later accessed, processed and plotted on the workstation.

Figure 16. A replication of the plots drawn on the workstation monitor during the experiment. This set depicts shot number 193, on the conventional ICCS. The 3-ampere heater pulse is barely visible in the upper left hand plot at $t = 0$. The zero-offset error in the pressure channel is evident in the lower right hand plot.

Figure 17. Replication of workstation monitor display for shot number 209, on the ICCS made with the dacron-sleeved cable. The background field and the initial transport current were the same for this shot as for the one in the previous figure.

Figures 18 and 19. These two figures represent the same two shots as did the previous two figures, but the data are presented differently. Voltage traces 2 through 5 are plotted together in these two figures in order to more easily discern their relative positions on the Time axis. Pressure data is redrawn relative to the initial pressure; that is, $\Delta P(t) = P(t) - P(0)$. Comparison of these two figures reveals the essential differences in behavior between the two samples.

Figure 20. Data from shot number 212. The background field for this shot was the same as for shot 209, but the initial transport current was higher, 3.5 kA vs. 3.0 kA. Of particular note are the higher slopes of the curves in the upper right hand plot, and the; higher peak pressure.

Figures 21 and 22. Data from shots 215 and 240; the background field was the same for these two shots, but the current for 240 was higher by a factor of 2.25. The higher slopes in the higher current case are clearly evident, as is the higher peak pressure. As indicated by knee in trace V5, the temperature of the entire length of conductor reached T_c in about 250 ms after the heat pulse, whereas in the lower current case, even trace V4 has failed to reach the T_c knee after nearly 2 seconds.

Figure 23. Data from shot 248 is very similar to that shown in the previous figure. The background field was lower, at 5 T, and the initial transport current was slightly higher, $\approx$ 5 kA compared to 4.5 kA in shot 240.

Figures 24 through 29. This series of six figures replots the data for the same six shots as power per unit length rather than as voltage per unit length, as described in detail in the text.

Figures 30 through 35. This series of six figures replots the data for the same six shots

as cumulative energy deposition per unit length rather than as voltage per unit length, as described in detail in the text.

5.0 References

1. Quarterly Progress Report, Oct. 1, 1984 to Dec. 31, 1984, Develop and Test an ICCS for Large Scale MHD Magnets, MIT, March 1985 DOE/PC-70512-2.
2. Technical Progress Report, period from Jan. 1, 1985 to June 30, 1985, Develop and Test an ICCS for Large Scale MHD Magnets, MIT, November 1985, DOE/PC-70512-4.
3. Analysis Report, Develop and Test an Internally Cooled Cabled Superconductor (ICCS) for Large Scale MHD Magnets, MIT, January 1986, DOE/PC-70512-5.
4. Thome, R.J. and Tarrh, J.M., *MHD and Fusion Magnets: Field and Force Design Concepts*, John Wiley and Sons, Inc. 1982.
5. E.S. Bobrov, P.G. Marston, E.N. Kuznetsov, Theoretical and Engineering Aspects of Momentless Structures and Coil End Turns in Superconducting MHD Magnets, *Adv. Cryo. Eng.*, Vol. 27, pp 47-55, 1982.
6. C.J. Heyne, D.T. Hackworth, S.K. Singh, Y.L. Young, Westinghouse Design of a Forced Flow Nb_3Sn Test Coil for the Large Coil Program, and references therein, Eighth Symposium On Engineering Problems in Fusion Research, pp 1148-1153, 1979.
7. Luongo, C. A., Loyd, R.J., Chen, F.K., Thermal-Hydraulic Simulation of Helium Expulsion from a Cable-in-Conduit Conductor, IEEE Trans. Mag., MAG-25(2):1589-1592, 1989.
8. Ando, T. et al., Propagation Velocity of the Normal Zone in a Cable-in-Conduit Conductor, preprint, 1989.